

UNIVERSITY PRESS

Research Article

Abundance analysis of chemically depleted post-AGB/post-RGB binaries with faint discs

Maksym Mohorian^{1,2}, Devika Kamath^{1,2,3}, Meghna Menon^{1,2}, Hans Van Winckel⁴, Mingjie Jian⁵, Anish M. Amarsi⁶ and Kateryna Andrych^{1,2}

¹School of Mathematical and Physical Sciences, Macquarie University, Sydney, NSW, Australia, ²Astrophysics and Space Technologies Research Centre, Macquarie University, Sydney, NSW, Australia, ³INAF, Osservatorio Astronomico di Roma, Monte Porzio Catone, Italy, ⁴Institute of Astronomy, KU Leuven, Leuven, Belgium, ⁵Department of Astronomy, Stockholm University, AlbaNova University Center, Stockholm, Sweden and ⁶Theoretical Astrophysics, Department of Physics and Astronomy, Uppsala University, Uppsala, Sweden

Abstract

Post-asymptotic giant branch (Post-AGB) and post-red giant branch (post-RGB) binaries with stable circumbinary discs provide key insights into late stellar and disc evolution, revealing how binary interactions shape disc structure and stellar surface composition. A defining trait of such systems is the observed underabundance of refractory elements in the stellar photosphere relative to volatile elements – photospheric chemical depletion – resulting from the star accreting volatile-rich circumstellar gas. In this study, we investigated the link between photospheric depletion and disc evolution by focusing on post-AGB/post-RGB binaries with low infrared excess (hereafter 'faint disc' targets). We analysed high-resolution optical spectra from HERMES/Mercator and UVES/VLT for 6 Galactic and 2 LMC targets. Using E-iSpec, we homogeneously derived atmospheric parameters and chemical abundances of 29 elements from carbon to europium, and included NLTE corrections for 15 elements from carbon to barium that we calculated using pySME and pre-computed grids of departure coefficients. All targets exhibit 'saturated' depletion patterns, which we characterised using two-piece linear fits defined by three parameters: initial metallicity ([M/H]₀), turn-off temperature ($T_{\text{turn-off}}$), and depletion scale ($\nabla_{100\,\text{K}}$). Among several findings, we highlight the bimodal distribution of $T_{\text{turn-off}} > 1\,100\,\text{K}$), and transition discs with inner clearing ($T_{\text{turn-off}} < 1\,100\,\text{K}$). Our results imply that faint disc targets likely represent the final stages of disc dissipation, highlighting the diversity of depletion profiles, the complexity of disc-binary interactions, and the need to understand the rarity and evolution of faint disc systems.

Keywords: Techniques: spectroscopic; stars: abundances; stars: AGB and post-AGB; stars: chemically peculiar; stars: evolution (Received 15 August 2025; revised 12 October 2025; accepted 17 October 2025)

1. Introduction

Post-asymptotic giant branch (post-AGB) and post-red giant branch (post-RGB) binaries with circumbinary discs (CBDs) offer a unique opportunity to study disc-binary interactions and their impact on stellar surface chemistry. Towards the end of the AGB phase, low- and intermediate-mass stars (0.8–8 $\rm M_{\odot}$) lose most of their envelope mass through stellar winds (van Winckel 2003; Kobayashi, Karakas, & Lugaro 2020; Kamath et al. 2023). In binary systems, the AGB/RGB phase can be prematurely terminated by mass loss, enhanced by poorly understood binary interactions (Paczyński 1971; van Winckel 2003). This process leads to the formation of a post-AGB or post-RGB primary star and the surrounding CBD (van Winckel 2003; Kamath et al. 2016; Van Winckel 2018).

The presence of CBDs around post-AGB and post-RGB binaries has been observationally confirmed through the detection of

Corresponding author: Maksym Mohorian; Email: maksym.mohorian@students.mq.edu.au

Cite this article: Mohorian M, Kamath D, Menon M, Van Winckel H, Jian M, Amarsi AM and Andrych K. (2025) Abundance analysis of chemically depleted post-AGB/post-RGB binaries with faint discs. *Publications of the Astronomical Society of Australia* 42, e151, 1–20. https://doi.org/10.1017/pasa.2025.10117

dust excess, which manifests as a broad near-infrared (near-IR) excess in their spectral energy distributions (SEDs) (de Ruyter et al. 2005; Kamath, Wood, & Van Winckel 2014, 2015, 2016; Gezer et al. 2015; Kluska et al. 2022). Detailed imaging studies have revealed complex dust structures within these discs, including cavities, rings, and arc-like features, through interferometric (Kluska et al. 2019; Corporaal et al. 2023) and polarimetric techniques (Ertel et al. 2019; Andrych et al. 2023, 2024). Additionally, the outer regions of CBDs exhibit signatures of dust crystallisation (Gielen et al. 2011b; Hillen et al. 2015), grain growth (Scicluna et al. 2020), and Keplerian rotation (Bujarrabal et al. 2015, 2018; Gallardo Cava et al. 2021, 2023; Alcolea et al. 2023).

Kluska et al. (2022) classified Galactic post-AGB/post-RGB binaries into five categories, depending on their near-IR H-K and mid-IR W_1-W_3 colours. Based on the IR colour-colour plot, targets with moderate mid-IR excess $(2.3^m < W_1-W_3 < 4.5^m)$ potentially host full discs, where dust distribution starts from the sublimation radius (Hillen et al. 2016, 2017; Kluska et al. 2018). In contrast, targets with high mid-IR excess $(W_1-W_3>4.5^m)$ and/or low near-IR excess $(H-K<0.4^m)$ potentially host transition discs, which display inner gaps or cavities in the dust distribution (Corporaal et al. 2023). Finally, targets with low IR excess $(H-K<0.4^m)$, $W_1-W_3<2.3^m)$ do not clearly fit into

© The Author(s), 2025. Published by Cambridge University Press on behalf of Astronomical Society of Australia. This is an Open Access article, distributed under the terms of the Creative Commons Attribution licence (https://creativecommons.org/licenses/by/4.0/), which permits unrestricted re-use, distribution and reproduction, provided the original article is properly cited.

the full or transition disc categories and remain less understood. Despite differences in IR excess, all categories show evidence of disc-binary interactions, although the mechanisms driving these interactions remain poorly understood (Heath & Nixon 2020; Penzlin et al. 2022). Observational signatures of these interactions include jet formation (results from interaction between the disc and the companion star, which is typically a main-sequence star Oomen et al. 2018; Verhamme et al. 2024; De Prins et al. 2024) and photospheric chemical depletion (arises from interaction between the disc and the post-AGB/post-RGB primary Oomen et al. 2019, 2020).

In this study, we focus on photospheric chemical depletion, which occurs when gas in the CBD becomes fractionated from dust and is subsequently re-accreted onto the post-AGB/post-RGB star, altering its observed surface composition (Van Winckel, Waelkens, & Waters 1995; Van Winckel 1997; Maas, Van Winckel, & Lloyd Evans 2005; Giridhar et al. 2005; Gezer et al. 2015; Oomen et al. 2019). The efficiency of gas-dust fractionation depends on the condensation properties of the gas mixture, commonly described by 50% condensation temperature $T_{\text{cond},50\%}^{\text{a}}$ (T_{cond} ; Lodders 2003; Wood, Smythe, & Harrison 2019; Agúndez et al. 2020). The fractionation process in the CBD separates gas containing elements with condensation temperatures $T_{\rm cond} \lesssim 1250$ K (volatile elements, including Na, S, Cu, and Zn) and dust containing elements with condensation temperatures $T_{\rm cond} \gtrsim 1\,250\,{
m K}$ (refractory elements, including Al, Si, Ti, Fe, and neutron capture process elements). Consequently, re-accreted volatile-rich matter dominates the original stellar surface composition, completely masking the nucleosynthetic products of AGB/RGB evolution (de Ruyter et al. 2005, 2006; Oomen et al. 2018). The resulting photospheric underabundance (depletion) of refractory elements in the post-AGB/post-RGB binaries is particularly prominent in the relative [X/H] abundance scale and is commonly plotted against T_{cond} (depletion profile; de Ruyter et al. 2005; Maas et al. 2005; Oomen et al. 2019).

Photospheric depletion in post-AGB/post-RGB binaries is commonly explored using four key parameters (Van Winckel 2018; Kluska et al. 2022):

- The turn-off temperature $T_{\rm turn-off}$, which marks the separation between weakly depleted and significantly depleted elements. In previous studies, this parameter was estimated visually (Oomen et al. 2019; Kluska et al. 2022).
- The initial metallicity [M/H]₀ ([S/H], [Zn/H], or their average, since Fe is depleted in post-AGB/post-RGB binaries), which traces the baseline composition of metals in the stellar surface. We note that volatile elements (including O, S, and Zn) may be mildly depleted (Mohorian et al. 2024, 2025).
- The volatile-to-refractory abundance ratio ([Zn/Ti], [Zn/Fe], or [S/Ti]), which provides a scale for the efficiency of depletion (Waelkens et al. 1991; Oomen et al.

- 2019, 2020). Based on [Zn/Ti] abundance ratios, post-AGB/post-RGB binaries can be categorised into four distinct groups: (i) mildly depleted ([Zn/Ti] \lesssim 0.5 dex), (ii) moderately depleted (0.5 dex \lesssim [Zn/Ti] \lesssim 1.5 dex), (iii) strongly depleted (1.5 dex \lesssim [Zn/Ti] \lesssim 2.5 dex), and (iv) extremely depleted ([Zn/Ti] \gtrsim 2.5 dex). We note that [Zn/Ti] abundance ratio depends on $T_{\text{turn-off}}$ and [M/H]₀.
- The abundance pattern of the most refractory elements $(T_{\rm cond} \gtrsim 1~400~{\rm K})$: (i) linear decline of [X/H] with increasing $T_{\rm cond}$ ('saturation') or (ii) near-constant [X/H] with increasing $T_{\rm cond}$ ('plateau'). The saturated and plateau profiles represent systems where the re-accreted matter is fully or partially diluted in the stellar photosphere, respectively (Oomen et al. 2019).

CNO elements (C, nitrogen N, and oxygen O) are commonly omitted from the depletion analyses of post-AGB/post-RGB binaries, since the surface abundances of CNO elements are significantly altered by nucleosynthetic and mixing processes during the AGB/RGB evolution (Oomen et al. 2019, 2020; Mohorian et al. 2024; Menon et al. 2024). For this reason, we similarly excluded CNO elements from our depletion analysis of post-AGB and post-RGB binaries.

The depletion efficiency of non-CNO elements is highly diverse across the post-AGB/post-RGB sample with different subtypes of CBDs: full disc targets generally show milder depletion ([Zn/Ti] $\lesssim 1$ dex), transition disc targets commonly display the strongest depletion ([Zn/Ti] $\gtrsim 2$ dex), and faint disc targets display a wide range of depletion efficiencies. However, we note that a small subset of full disc targets displays extremely low metallicity ([Fe/H] \lesssim –3 dex). This subset includes Red Rectangle, AG Ant, PS Gem, and HP Lyr (Kluska et al. 2022), and the physical mechanisms behind the extreme depletion of Fe and other refractory elements in these full disc targets remain uncertain.

Furthermore, photospheric depletion is not limited to post-AGB and post-RGB binaries; a similar phenomenon was observed in young planet-hosting stars (λ Böo phenomenon; Venn & Lambert 1990; Andrievsky et al. 2002; Jura 2015; Murphy et al. 2020). The depletion profiles in stars showing λ Böo phenomenon suggest a possible connection between depletion mechanisms and the processes of planet formation (Kama, Folsom, & Pinilla 2015; Jermyn & Kama 2018). Similarly, the depletion profiles in post-AGB/post-RGB binaries with transition discs were proposed to stem from second-generation planet formation in their CBDs (Kluska et al. 2022).

To investigate how the diversity of photospheric depletion profiles is affected by the CBDs around post-AGB/post-RGB binaries, the nature of different disc types needs to be understood. In our previous studies, we homogeneously explored the depletion profiles of subsets of targets hosting full and transition discs (Mohorian et al. 2024, 2025). In this study, we focus on a subset of post-AGB and post-RGB binaries with low IR excess, corresponding to category 4 in the classification scheme of Kluska et al. (2022). We refer to these as faint disc targets. Unlike full and transition disc targets, faint disc systems lack strong near- or midinfrared excess, yet still show chemical evidence of disc-binary interaction. By analysing the chemical abundance profiles of faint disc targets and comparing them with previously studied full and transition disc systems, we aim to place faint disc targets within an evolutionary context. We propose three possible explanations for why these discs appear faint: (i) a reduced pressure scale height,

^aAt 50% condensation temperature for a selected element, half of the element by abundance is in the gas phase, while another half is in the dust phase. These condensation temperatures are commonly calculated for solar mixture gas in chemical equilibrium at pressure $P = 10^{-4}$ bar, so these temperatures should not be considered absolute. Nevertheless, all targets analysed in this study are oxygen-rich (0.07 < C/O < 0.81; see Section 3.2), with C/O ratios close to the solar value $(C/O_{\odot} \sim 0.6$; Asplund, Amarsi, & Grevesse 2021), implying that the major condensates should be the same (e.g. corundum, olivines, pyroxenes; Agúndez et al. 2020).

Table 1. General details regarding faint disc sample (names, coordinates, and photometric selection criteria; see Section 2.1). H and K magnitudes originate from the 2MASS 6X catalogue, while the W_1 and W_3 magnitudes are sourced from the AllWISE catalogue (see Section 2.2).

	Names		Coord	linates	Selection criteria		
Adopted	IRAS/OGLE	IRAS/OGLE 2MASS		Dec.	—————————————————————————————————————	$W_1 - W_3$	
			(deg)	(deg)	(mag)	(mag)	
Galactic targets							
SS Gem	06054+2237	J06083510+2237020	092.146283	+22.617229	$\boldsymbol{0.190 \pm 0.060}$	$\textbf{0.886} \pm \textbf{0.119}$	
V382 Aur	06338+5333	J06375242+5331020	099.468426	+53.517227	$\boldsymbol{0.078 \pm 0.035}$	$\boldsymbol{2.239 \pm 0.050}$	
CC Lyr	-	J18335741+3138241	278.489225	+31.640045	$\boldsymbol{0.167 \pm 0.041}$	$\boldsymbol{1.826 \pm 0.041}$	
R Sct	18448-0545	J18472894-0542185	281.870622	-05.705157	$\textbf{0.218} \pm \textbf{0.528}$	$\boldsymbol{1.061 \pm 0.324}$	
AU Vul	20160+2734	J20180588+2744035	304.524513	+27.734322	$\textbf{0.364} \pm \textbf{0.066}$	$\boldsymbol{1.301 \pm 0.136}$	
BD+39 4926	-	J22461123+4006262	341.546798	+40.107304	$\boldsymbol{0.056 \pm 0.034}$	$\textbf{0.668} \pm \textbf{0.040}$	
LMC targets							
J052204	LMC-LPV-46487	J05220425-6915206	80.517725	-69.255730	$\textbf{0.056} \pm \textbf{0.100}$	$\boldsymbol{2.257 \pm 0.068}$	
J053254	LMC-T2CEP-149	J05325445-6935131	83.226904	-69.586983	$\boldsymbol{0.085 \pm 0.067}$	0.749 ± 0.083^{a}	

Notes: ${}^a[3.6]$ -[8.0] from SAGE catalogue (Woods et al. 2011) was adopted as mid-IR colour for J053254. By scaling to WISE wavelengths ($\lambda_{W_1}=3.368\,\mu\text{m},\,\lambda_{W_3}=12.082\,\mu\text{m}$), we estimate $W_1-W_3\sim1.5^m$ for this target, which constitutes as low mid-IR excess (below the cut-off magnitude of 2.3^m ; see Section 2.1).

suggesting gas-poor conditions due to the settling of large grains into the midplane, and (ii) a reduced dust content, as IR excess alone does not directly trace the total dust mass, or (iii) a combination of dust settling in the midplane and dust reduction in the disc (van Winckel 2003; van Winckel et al. 2009; Tosi et al. 2022; Dell'Agli et al. 2023).

The structure of the paper is as follows. In Section 2, we describe our target sample, data, and observation details. In Section 3, we outline the methodology and results of our chemical analysis of faint disc targets. In Section 4, we discuss photospheric depletion in faint disc targets and its connection to CBD evolution. Finally, in Section 5, we summarise the key findings of this study.

2. Sample, data, and observations

In this study, we focus on a subset of post-AGB/post-RGB binary stars with faint discs. In Section 2.1, we present the target sample and explain the selection criteria. In Section 2.2, we present the photometric data used to derive luminosities of our target sample (using SED fitting and PLC relation; see Section 3.1). In Section 2.3, we briefly discuss the spectroscopic data used to derive precise atmospheric parameters and elemental abundances of the faint disc targets (using E-iSpec and pySME; see Section 3.2).

2.1 Sample selection

The initial target sample consisted of post-AGB and post-RGB binary stars in the Galaxy (Kluska et al. 2022) and the Magellanic Clouds (from Kamath et al. 2014, 2015). The binarity of the targets in the initial sample was either established through orbital solutions derived from long-term spectroscopic monitoring or indirectly inferred from chemical depletion patterns, which are characteristic signatures of binary interaction (van Winckel 2003; de Ruyter et al. 2006). From this initial sample of 85 Galactic targets, 28 SMC targets, and 91 LMC targets, we selected faint disc targets based on their IR magnitudes from the 2MASS Long

Exposure (6X) Full Survey (Cutri et al. 2012) and the AllWISE catalogue (Cutri et al. 2021), using the selection criteria $H - K < 0.4^m$ and $W_1 - W_3 < 2.3^m$ adopted from Kluska et al. (2022).

We further refined our target selection by only retaining objects with spectral types A to K for which we had high-resolution optical spectra (see Section 3.2). These spectral types allow for the optimal identification of Fe I and Fe II spectral features. As a result, BD+15 2862 was removed from our sample (spectral type B9, $T_{\rm eff} \sim 12\,000$ K; Giridhar & Arellano Ferro 2005). Additionally, we excluded an LMC object, MACHO 47.2496.8 (OGLE LMC-T2CEP-015), due to the observed enhancement of slow neutron capture process (s-process) elements in this target (Reyniers et al. 2007; Kamath et al. 2014; Menon et al. 2024). Menon et al. (2024) suggested that the depletion process (characteristic of our sample) is inhibited or absent in MACHO 47.2496.8, indicating that this target follows a different evolutionary pathway and is therefore not suitable for our study. As a result, our final target sample consists of 8 post-AGB/post-RGB binaries - 6 in the Galaxy and 2 in the LMC. For SS Gem, V382 Aur, and BD+39 4926, binary nature is confirmed by the measured orbital parameters (see Table 2). For 5 other faint disc targets, binarity is inferred based on the observed chemical depletion patterns - a well-established signature of binarity in post-AGB/post-RGB stars (see Section 1). In addition, the [Zn/Ti] abundance ratios within the sample (commonly used as a tracer of depletion efficiency; Van Winckel, Mathis, & Waelkens 1992; van Winckel 2003; de Ruyter et al. 2006; Gielen et al. 2009; Gorlova et al. 2012; Oomen et al. 2019; Kluska et al. 2022) vary from 0.2 dex for R Sct to $\gtrsim 3$ dex for CC Lyr.

We note that most of the faint disc targets (except for BD+39 4926) are classified as RV Tauri pulsating variables. For all such targets, we derived luminosities using the period-luminosity-colour (PLC) relation (see Section 3.1). In Table 1, we present the names, coordinates, and IR colours of our final sample of faint disc targets. In Figure 1, we show the IR colours of 8 faint disc targets from this study (marked by blue squares; for more details, see Section 4.1). In Table 2, we provide relevant literature data for our faint disc sample, including orbital and pulsational parameters, luminosities, and depletion parameters (for more details, see Appendix A).

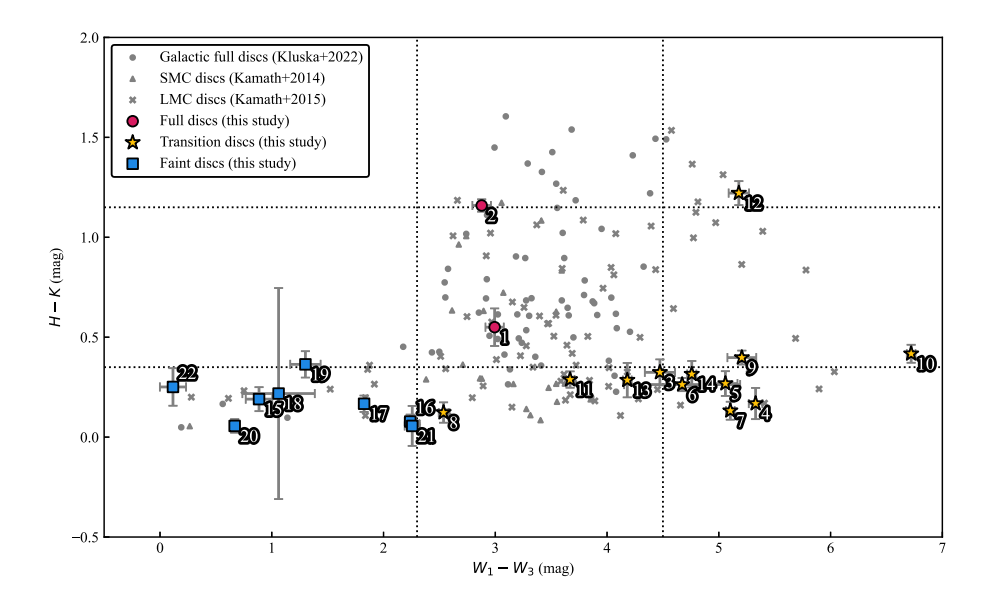


Figure 1. Updated IR colour-colour plot of post-AGB/post-RGB binary stars in the Galaxy and in the Magellanic Clouds. NIR magnitudes (H and H) are adopted from 2MASS 6X, while MIR magnitudes (H and H) are adopted from AllWISE (for more details, see Section 2.2). Grey markers represent the extended sample of post-AGB/post-RGB binaries in the Galaxy (circles; Kluska et al. 2022), in the Small Magellanic Cloud (triangles; Kamath et al. 2014), and in the Large Magellanic Cloud (crosses; Kamath et al. 2015). Coloured markers represent the post-AGB/post-RGB binaries homogeneously studied with E-iSpec+pySME (for more details, see Section 4.1): red circles mark the full disc targets (Mohorian et al. 2024), yellow stars mark the transition disc targets (Mohorian et al. 2025), and blue squares mark the faint disc targets (this study). Adopted contours represent the demarcation between different categories of disc targets (see Section 1; Kluska et al. 2022).

2.2 Photometric data

To construct SEDs, we compiled photometric magnitudes spanning the optical to far-IR wavelength range (see Table 3). This includes UBVRI photometry in the Johnson-Cousins system (Johnson & Morgan 1953; Cousins 1976); B_T and V_T bands from the Tycho-2 catalogue (Høg et al. 2000); I' band from the SDSS (York et al. 2000); J, H, and K magnitudes from 2MASS (Skrutskie et al. 2006); mid-IR W_1 to W_4 bands from WISE (Wright et al. 2010), and far-IR fluxes from AKARI, IRAS, PACS, and SPIRE (Ishihara et al. 2010; Neugebauer et al. 1984; Poglitsch et al. 2010; Griffin et al. 2010). For BD+28 772, ultraviolet magnitudes from 156.5 to 274 nm were also adopted from the TD1 catalogue (Thompson et al. 1978).

2.3 Spectroscopic data

In this subsection, we present the high-resolution optical spectra used in this study, obtained with HERMES/Mercator (Raskin et al. 2011; Gorlova et al. 2011) and UVES/VLT (Dekker et al. 2000). In Table 4, we present the observational log with measured radial velocities and periodicities in the spectra. To determine the radial velocities for all spectral visits of each faint disc target, we used E-iSpec (see Section 3.2). To analyse periodic variations in the derived radial velocity curves, we first applied the Lomb-Scargle periodogram to identify significant periodic signals (Lomb 1976; Scargle 1982), and then refined these periods using the Lafler-Kinman method (Lafler & Kinman 1965).

To derive precise atmospheric parameters and elemental abundances for our faint disc targets, we selected spectra in the following way (see Table 4):

• For targets observed with HERMES, we selected optical visits with the highest S/N ratios for each target.

 For targets observed with UVES, we combined all available spectral visits.

In Appendix B, we provide details of all the spectral visits considered. In Figure 2, we show the sample spectra of faint disc targets in the wavelength region near the S and Zn lines to illustrate the quality of our obtained data. We note that [S/H] and [Zn/H] abundances are commonly used to represent the initial metallicity [M/H]₀ of post-AGB/post-RGB binaries, rather than [Fe/H] abundance, due to the high efficiency of refractory depletion (see Section 1).

3. Derivation of luminosities, atmospheric parameters, and elemental abundances of faint disc targets

In this section, we discuss the methodology and results of the photometric and spectral analysis of faint disc targets. In Section 3.1, we outline the derivation of luminosities using SED fitting and PLC relation, based on the collected photometric data. In Section 3.2, we present the derivation of precise atmospheric parameters and elemental abundances using high-resolution optical spectra. In Section 3.3, we describe the calculation of non-local thermodynamic equilibrium (statistical equilibrium, NLTE) corrections, which significantly impact the chemical analysis of post-AGB/post-RGB binaries. In Section 3.4, we present the depletion profiles of faint (this study), transition (Mohorian et al. 2025), and full disc targets (Mohorian et al. 2024).

3.1 Luminosity estimation using SED fitting and PLC relation

In this study, we derived the luminosities of our target sample using the following methods: (i) SED fitting to calculate the SED

Table 2. Parameters of faint disc sample, including orbital, pulsational, and depletion parameters, as well as luminosity estimates adopted from the literature (see Section 2).

	Orbital ¡	parameters	Pulsatio parame	· · · · · · · · · · · · · · · · · · ·		Depletion parameters			
Name	P_{orb}	e	$P_{ m puls}$	RVb	$L_{ m SED}$	$L_{\rm IR}/L_*$	[Zn/Ti]	$T_{\rm turn-off}$	Profile
	(d)		(d)		(<i>L</i> _⊙)		(dex)	(K)	pattern
SS Gem	910°	-	44.525 ^a	yes	$4540\pm 1190^{\rm m}$	0.01 ^m	2.02 ^g	1 100	S
V382 Aur	$597.4 \pm 0.2^{\text{b}}$	$0.30\pm0.02^{\text{b}}$	29.06 ^c	yes	$3540\pm810^{\mathrm{m}}$	0.02^{m}	0.87 ^h	800	Р
CC Lyr	_	_	23.634 ^d	no	$650\pm210^{\rm m}$	0.03 ^m	$\gtrsim 3^{\rm i}$	1 000	S
R Sct	-	-	70.8 ^e	no	$2830\pm580^{\mathrm{m}}$	0.03 ^m	0.17 ^j	-	N
AU Vul	-	-	71.55 ^a	no	$4220\pm1160^\mathrm{m}$	0.06 ^m	-	-	-
BD+39 4926	$871.7\pm0.4^{\rm b}$	$0.024\pm0.006^{\mathrm{b}}$	-	no	$6120\pm1870^{\rm m}$	$> 0.00^{\rm m}$	2.03 ^k	1 000	S
J052204	-	-	30.172 ^f	no	$4170\pm970^{\rm n}$	0.02°	-	-	-
J053254	-	-	42.744 ^f	no	$3210\pm1210^\mathrm{n}$	>0.00°	0.6^{l}	-	-

Notes: The parameters are adopted from the following studies: a Pawlak et al. (2019), b Oomen et al. (2018), c Hrivnak et al. (2008), d Zong et al. (2020), e Kalaee & Hasanzadeh (2019), f Soszyński et al. (2008), g Gonzalez et al. (1997), h Hrivnak et al. (2008), i Maas et al. (2007), i Giridhar et al. (2000), k Rao et al. (2012), i Gielen et al. (2009), m Kluska et al. (2022), n Manick et al. (2018), o This study. For BD+39 4926 and J053254, the IR-to-stellar luminosity ratios are in the range $0 < L_{\rm IR}/L_* < 0.01$. $T_{\rm turn-off}$ and profile patterns are adopted from Oomen et al. (2019): 'S' means 'saturated', 'P' means 'plateau', 'N' means 'not depleted'.

Table 3. Photometric data of faint disc sample (see Section 2.2). The table includes units and central wavelengths (in μ m) for each filter. This table is published in its entirety in the electronic edition of the paper. A portion is shown here for guidance regarding its form and content.

Filter	 JOHNSON.B (I/280B/ascc)	 2MASS.J (II/246/out)	
Unit	 mag	 mag	
λ (μ m)	 0.443	 1.239	
SS Gem	 10.298 ± 0.052	 6.743 ± 0.032	
V382 Aur	 9.557 ± 0.019	 7.805 ± 0.020	
CC Lyr	 13.000 ± 0.259	 10.832 ± 0.019	
R Sct	 -	 2.824 ± 0.274	
AU Vul	 12.312 ± 0.165	 7.183 ± 0.026	

luminosities $L_{\rm SED}$ and (ii) PLC relation to obtain the PLC luminosities $L_{\rm PLC}$. In this subsection, we detail the procedures used for each method.

To calculate L_{SED} , we followed the procedure outlined in Mohorian et al. (2024). In brief, we fitted photometric data with spectra synthesised from Kurucz ODFNEW model atmospheres (Castelli & Kurucz 2003), integrating the bolometric IR luminosity and correcting for total reddening (interstellar and circumstellar; see Degroote et al. 2013). χ^2 minimisation was performed until the convergence of effective temperature $T_{\rm eff}$, surface gravity $\log g$, extinction (reddening) E(B-V), and stellar angular size θ . In our calculations, interstellar reddening follows the extinction law from Cardelli et al. (1989) with $R_V = 3.1^m$. We note that we used the Bailer-Jones geometric distances (z_{BJ}) with Gaia EDR3 parallaxes (Bailer-Jones et al. 2021), assuming isotropic radiation emission. Additionally, we did not explicitly account for pulsational variability, which resulted in higher χ^2 values for pulsating variables. The uncertainties in L_{SED} are mainly caused by uncertainties in distance and reddening. In Figure 3, we show the SEDs of faint disc targets.

We note that the IR excess of faint disc targets is not only weak in flux contribution (0 < $L_{\rm IR}/L_*$ < 0.1), but also generally starts at \sim 10 μ m (for V382 Aur and CC Lyr, at \sim 5 μ m). This

is significantly different from the IR excesses of full and transition disc systems, which start at \sim 1 μm and \sim 3 μm , respectively (Kluska et al. 2022).

To calculate $L_{\rm PLC}$, we applied the calibrated relation described in Menon et al. (2024), given by

$$M_{bol} = m_{cal} \cdot \log P_0 + c_{cal} - \mu + BC + 2.55 \cdot (V - I)_0,$$
 (1)

where M_{bol} is the absolute bolometric magnitude; $m_{cal} = -3.59^m$ and $c_{cal} = 18.79^m$ are the calibrated slope and intercept of PLC relation, respectively; P_0 is the observed fundamental period of pulsation; $\mu = 18.49$ is the distance modulus to the LMC (used to calibrate the relation); BC is the bolometric correction based on the $T_{\rm eff}$ (Flower 1996; Torres 2010); and $(V-I)_0$ is the intrinsic (de-reddened) colour based on the reddening value E(B-V) from the SED fit. The uncertainties in $L_{\rm PLC}$ are mainly caused by uncertainties in E(B-V).

We note that $L_{\rm PLC}$ provides a more reliable luminosity estimate than $L_{\rm SED}$, since $L_{\rm SED}$ is more sensitive to model fitting variations caused by RV Tau pulsations (Menon et al. 2024). Therefore, for all pulsating variables in the faint disc sample, we use $L_{\rm PLC}$ as the adopted luminosity for our subsequent analysis. For the nonpulsating star, BD+39 4926, we adopt $L_{\rm SED}$ instead. In Table 5, we provide the derived values and uncertainties for both $L_{\rm SED}$ and $L_{\rm PLC}$.

3.2 Derivation of atmospheric parameters and elemental abundances using E-iSpec

In this study, we derived atmospheric parameters and elemental abundances using E-iSpec, a semi-automated spectral analysis code (Mohorian et al. 2024), specifically tailored for evolved stars with complex atmospheres. E-iSpec is a modified version of the iSpec spectral analysis code (Blanco-Cuaresma et al. 2014; Blanco-Cuaresma 2019). The analysis within E-iSpec is conducted using the LTE Moog transfer code (operating with equivalent width method, Sneden et al. 2012), the VALD3 line list (Kupka, Dubernet, & VAMDC Collaboration 2011), solar abundances from Asplund et al. (2021), and 1D plane-parallel ATLAS9 model atmospheres (Castelli & Kurucz 2003). In Appendix C, we

Table 4. Analysed spectral visits of faint disc targets. For more details on the criteria used for selecting spectral
visits, see Section 2.3. For a complete observational summary of faint disc targets, see Appendix B.

Name	Facility	ObsID	MJD	RV (km/s)	S/N	P_{RV} (d)
SS Gem	H/M	273787,	55232.98736,	-15.8	45	44.66
		273788,	55232.99957,			
		273789	55233.01175			
V382 Aur	H/M	904077,	58450.08702,	-84.6	65	599.1
		904090	58450.20395			
CC Lyr	H/M	356745,	55723.94027,	-35.8	55	23.69
		356746,	55723.96863,			
		356747	55723.99005			
R Sct	H/M	972206	59073.92861	36.2	35	71.54
AU Vul	H/M	596805,	56935.86608,	-2.1	35	75.84
		596806	56935.88750			
BD+39 4926	H/M	244722,	55067.06677,	-15.8	80	879.0
		244722,	55067.06677,			
J052204	U/V	456+472,	58451.31574,	231.3	45	-
		739+776	58470.18473			
J053254	U/V	494	53409.20586	268.8	40	-

Notes: H/M denotes HERMES/Mercator, and U/V denotes UVES/VLT. RV is the radial velocity of the spectrum used in the analyses (for merged spectral visits, the range of RVs is < 0.5 km/s). S/N is the average signal-to-noise ratio of the spectrum. $P_{\rm RV}$ is the period derived from RV curves, initially estimated using a Lomb-Scargle periodogram and refined with the Lafler-Kinman method.

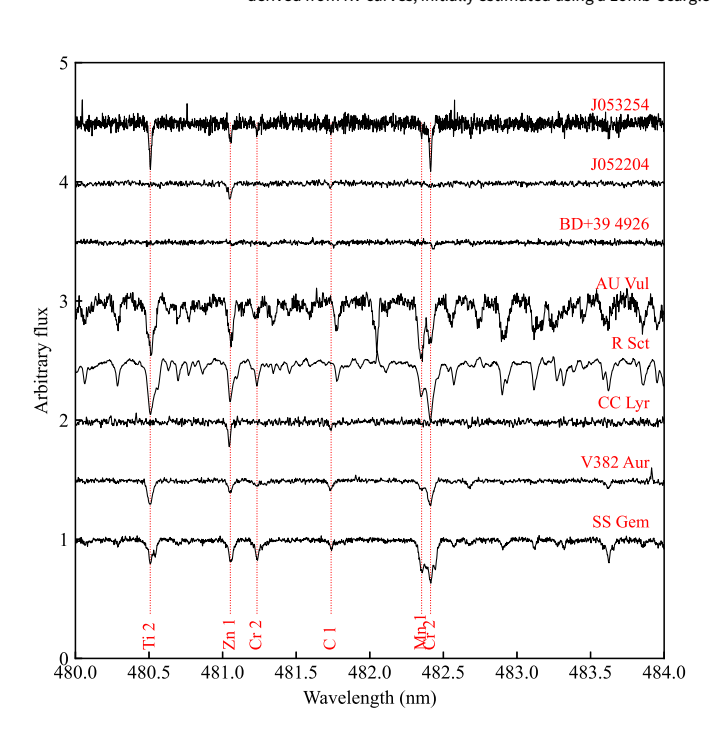


Figure 2. Spectra of all faint disc targets across the region featuring lines from the volatile S and Zn. Each spectrum is RV corrected, normalised, and offset in flux for clarity. Red dashed vertical lines mark the positions of spectral line peaks (for more details, see Section 3.2).

present the final line list selected for the precise derivation of atmospheric parameters and elemental abundances.

For atmospheric parameters, we adopt the original iSpec method for computing uncertainties. For elemental abundances, we compute the uncertainties using a quadrature sum of random and systematic components (for more details, see Mohorian et al. 2025). We note that the random component is set to 0.1 dex for elements with abundance derived from a single spectral line. Additionally, we assume that variations in metallicity affect the [X/Fe] abundance ratios, but not the [X/H] abundances.

In Table 5, we present the derived atmospheric parameters and selected elemental abundance ratios of faint disc targets ([Zn/Ti], [Zn/Fe], [S/Ti], and C/O). In Figures 4 and 5, we mark the derived LTE abundances with cyan circles. In Appendix D, we present the derived LTE [X/H] abundances of faint disc targets.

3.3 Calculation of NLTE corrections using pySME

Departures from LTE generally (but not always) increase with higher $T_{\rm eff}$ and decreasing [Fe/H], particularly for weak lines of neutral minority species, including Fe I and Ti I, because of the stronger UV radiation field that can drive overionisation (e.g. Lind & Amarsi 2024). The departures also tend to increase with lower log g owing to less efficient collisional processes that would bring the system closer to LTE. As such, NLTE effects are important to consider when characterising most post-AGB/post-RGB stars ($T_{\rm eff} \gtrsim 6\,000$ K, $\log g \lesssim 1$ dex, [Fe/H] $\lesssim -1.5$ dex).

In this study, we expand our NLTE analysis beyond that of Mohorian et al. (2025). Previously, in Mohorian et al. (2025), we used Balder (Amarsi et al. 2018) to calculate NLTE corrections for individual spectral lines of C, N, O, Na, Mg, Al, Si, S, K, Ca, and Fe by matching the LTE and NLTE equivalent widths. In this work, we performed a more extensive analysis by adding Ti, Mn, Cu, and Ba to the list of NLTE-corrected elements. This scaling-up was motivated by the need to enhance the coverage of the depletion profiles for our targets, and therefore demanded a more efficient computational approach. We opted to use the 1D pySME code (Wehrhahn, Piskunov, & Ryabchikova 2023), which has the functionality to generate NLTE spectra with the help of grids of departure coefficients $\beta_k = \frac{\eta_k^{\text{NLTE}}}{\eta_k^{\text{LTE}}}$ (pre-computed in

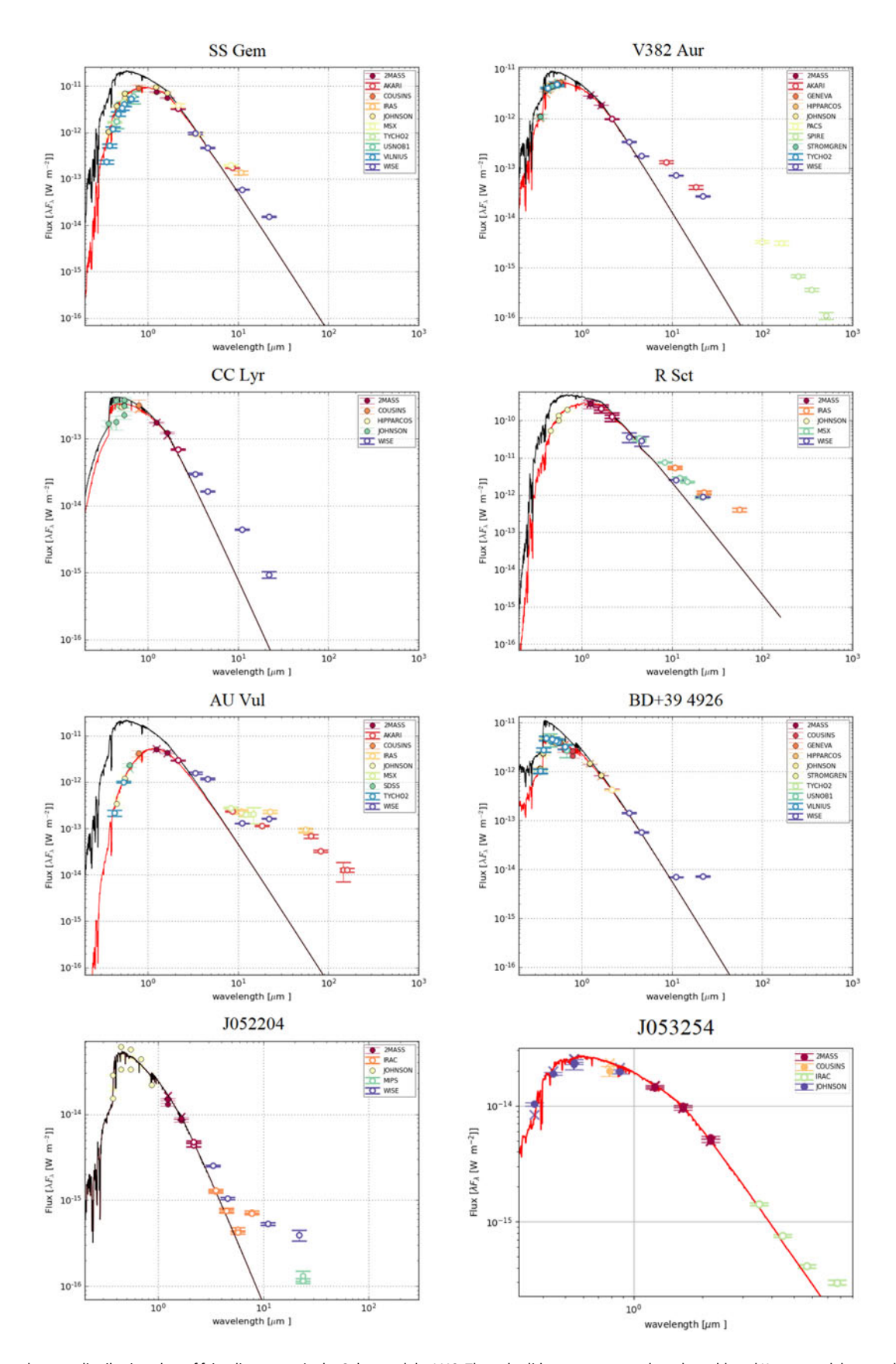


Figure 3. Spectral energy distribution plots of faint disc targets in the Galaxy and the LMC. The red solid curve corresponds to the reddened Kurucz model atmosphere, while the black solid curve represents Kurucz model atmosphere after de-reddening and scaling to the object. A legend within the plot clarifies the meaning of the symbols and colours used.

Table 5. Derived luminosities, atmospheric parameters, selected abundances and abundance ratios of faint disc targets (see Sections 3.1 and 3.2). For a full list of [X/H] abundances, see Appendix D.

	Derived luminosities			Atmospheric parameters			LTE ratios		NLTE ratios	
Target	$\log \frac{L_{\text{SED}}}{L_{\odot}}$	$\log \frac{L_{\rm PLC}}{L_{\odot}}$	$T_{ m eff}$	$\log g$	[Fe/H]	ξt	[Zn/Ti]	[Zn/Fe]	[S/Ti]	C/O
			(K)	(dex)	(dex)	(km/s)	(dex)	(dex)	(dex)	
SS Gem	3.657 ± 0.116	$3.400^{+0.099}_{-0.296}$	6500 ± 90	1.96 ± 0.11	-1.02 ± 0.12	4.08 ± 0.09	0.98 ± 0.21	0.45 ± 0.25	1.25 ± 0.09	0.55 ± 0.28
V382 Aur	3.549 ± 0.101	$3.350^{+0.113}_{-0.183}$	6020 ± 150	0.38 ± 0.27	-1.82 ± 0.08	4.14 ± 0.13	0.81 ± 0.34	0.69 ± 0.31	1.64 ± 0.19	0.38 ± 0.13
CC Lyr	2.811 ± 0.143	$2.986^{+0.211}_{-0.099}$	6470 ± 250	1.64 ± 0.50	-3.80 ± 0.03	4.14 ± 1.00	_	2.95 ± 0.44	_	0.03 ± 0.02
R Sct	3.452 ± 0.090	$3.099^{+0.113}_{-0.394}$	5630 ± 70	0.93 ± 0.11	-0.60 ± 0.11	2.93 ± 0.03	0.54 ± 0.17	0.42 ± 0.17	0.31 ± 0.13	0.17 ± 0.04
AU Vul	3.626 ± 0.123	$3.816^{+0.253}_{-0.141}$	4740 ± 40	0.00 ± 0.09	-0.95 ± 0.08	4.32 ± 0.04	0.40 ± 0.27	0.08 ± 0.36	_	0.07 ± 0.00
BD+39 4926	3.787 ± 0.137	_	7470 ± 40	0.52 ± 0.05	-2.37 ± 0.18	2.21 ± 0.25	2.69 ± 0.44	2.17 ± 0.29	3.36 ± 0.35	0.14 ± 0.10
J052204	3.620 ± 0.091	$3.307^{+0.225}_{-0.000}$	7020 ± 100	1.65 ± 0.11	-2.49 ± 0.10	2.36 ± 0.04	3.15 ± 0.34	1.98 ± 0.33	_	0.54 ± 0.21
J053254	3.507 ± 0.139	$3.843^{+0.070}_{-0.479}$	6040 ± 90	0.47 ± 0.13	-1.66 ± 0.09	2.36 ± 0.03	0.87 ± 0.27	0.45 ± 0.23	1.31 ± 0.15	0.81 ± 0.21

Note: We adopt $L_{\rm PLC}$ for all targets except BD+39 4926 and BD+28 772, for which we adopt $L_{\rm SED}$.

Balder for each energy level k with population n_k ; Amarsi et al. 2020). Since the departure coefficients used in pySME were calculated for MARCS model atmospheres (Gustafsson et al. 2008), which are limited for hot metal-poor giants, we set $T_{\rm eff} = 5\,750\,{\rm K}$ and/or $\log g = 0.5$ dex in NLTE calculations for all targets with higher $T_{\rm eff}$ and lower $\log g$, respectively. In Table 6, we list the references for the model atoms used to calculate the departure coefficient grids. The NLTE corrections were determined as the differences between the NLTE and LTE abundances, as explained below.

To calculate NLTE abundances, we synthesised the LTE spectral lines in pySME using observed equivalent widths and derived LTE atmospheric parameters. Then, we fitted these lines with NLTE spectral lines. The differences between NLTE and LTE abundances derived from the pySME fitted lines provided the relative abundance correction $\Delta_i^{\text{diff.}} = [\text{X/H}]_i^{\text{NLTE}} - [\text{X/H}]_i^{\text{LTE}}$ for each studied spectral line *i* (for average values of these corrections, see Section 4.1). To calculate the uncertainty of NLTE abundance for an ionisation of an element, we added in quadratures the systematic uncertainty of LTE abundance (abundance deviations within the error bars of atmospheric parameters) and random uncertainty of individual NLTE abundances (0.1 dex for single line, standard deviation for more lines).

In Appendix D, we provide the derived NLTE [X/H] abundances of faint disc targets. In Figures 4 and 5, we present 'NLTE-insensitive' abundances (V II and Cr II; navy triangles) and NLTE-corrected abundances (pink squares) of faint disc targets. In Appendix E, we show that NLTE corrections have a minor impact on general trends in depletion profiles, although these corrections are essential for the derivation of precise individual abundances.

3.4 Quantification of depletion efficiency using three free parameters

Depletion efficiency is measured primarily using volatile-to-refractory abundance ratios, including [Zn/Ti], [Zn/Fe], and [S/Ti] ratios (see Section 1). Although these abundance ratios allow for comparison with the literature, they do not fully determine which elements are significantly affected by depletion. Another depletion parameter, $T_{\rm turn-off}$ was traditionally determined by visual inspection, making it subjective and difficult to apply consistently. Furthermore, the high-temperature end of the

depletion profile used to be categorised as 'saturated' or 'plateau' pattern (see Section 1). Although this pattern classification is intuitive, it lacks a quantitative basis and does not allow direct comparisons between different systems.

In Table 5, we present [Zn/Ti], [Zn/Fe], and [S/Ti] ratios of faint disc targets (see Section 3.2). We note that we used NLTE-corrected abundances of S, Ti, and Fe to derive these volatile-to-refractory abundance ratios (see Section 3.3). In Table 2, we provide the reported $T_{\rm turn-off}$ values for faint disc targets from literature studies. In Table 2, we list the reported patterns of depletion profiles for faint disc targets from literature studies.

In this study, we investigated the efficiency of depletion in post-AGB/post-RGB binaries by exploring the shape of the depletion profiles (see Figures 4 and 5). To achieve this goal, we introduce a new approach to quantify depletion efficiency by fitting depletion profiles with two-piece linear functions, which have three free parameters:

- The break of the two-piece linear function separates weakly and significantly depleted elements (elements with lower and higher condensation temperatures, respectively; see Section 1) and is represented by the turn-off temperature $T_{\rm turn-off}$.
- The left linear piece has a zero slope and describes the abundances of weakly depleted elements with $T_{\rm cond} < T_{\rm turn-off}$ ([X/H] = [M/H]₀, where [M/H]₀ is the initial metallicity).
- The right linear piece describes the abundances of significantly depleted elements with $T_{\rm cond} \geq T_{\rm turn\text{-}off}$ ([X/H] = [M/H]₀ + $\nabla_{100\,\mathrm{K}} \cdot \frac{T_{\rm cond} T_{\rm turn\text{-}off}}{100\,\mathrm{K}}$, where $\nabla_{100\,\mathrm{K}}$ is the depletion scale in dex per 100 K).

The observed depletion profiles were fitted using a Bayesian approach implemented in PyMC5, using the No-U-Turn Sampler (NUTS) with 4 chains of 10 000 tuning and 10 000 sampling iterations each. The priors were placed on the model parameters as follows: initial metallicity [M/H]₀ and depletion scale $\nabla_{100\,\mathrm{K}}$ were assigned normal distributions centered at 0 dex with a standard deviation of 10 dex, while turn-off temperature $T_{\mathrm{turn-off}}$ was given a uniform distribution spanning the full temperature range of each individual depletion profile (excluding CNO elements; see Section 1). Parameter uncertainties were modelled

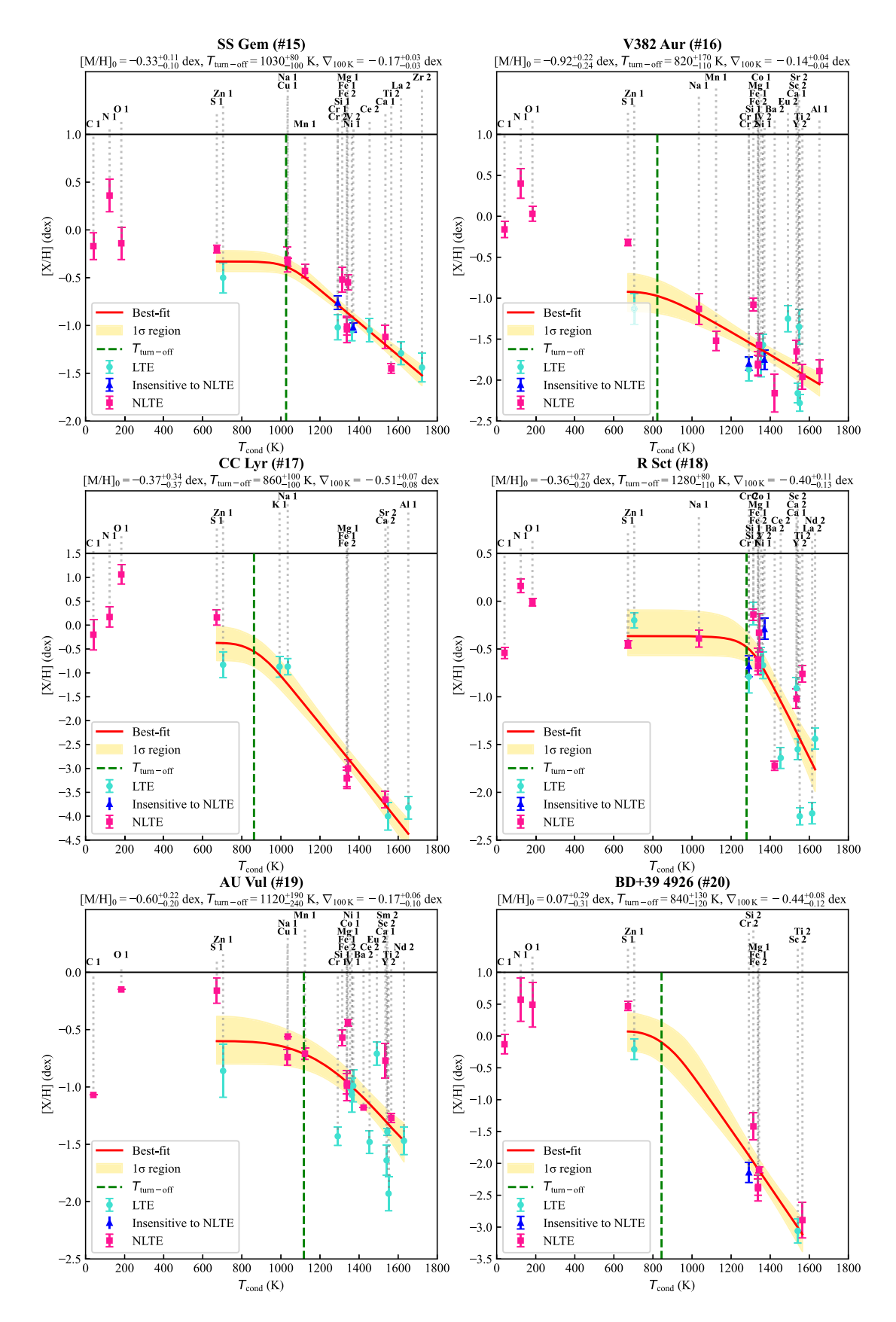


Figure 4. Elemental abundances of a subsample of post-AGB/post-RGB binaries with faint discs as functions of condensation temperature (Lodders 2003; Wood et al. 2019). For ID explanation, see Table 7. The legend for the symbols and colours used is included within the plot. 'NLTE insensitive' abundances are derived from spectral lines of V II and Cr II; for more details, see Section 3.2).

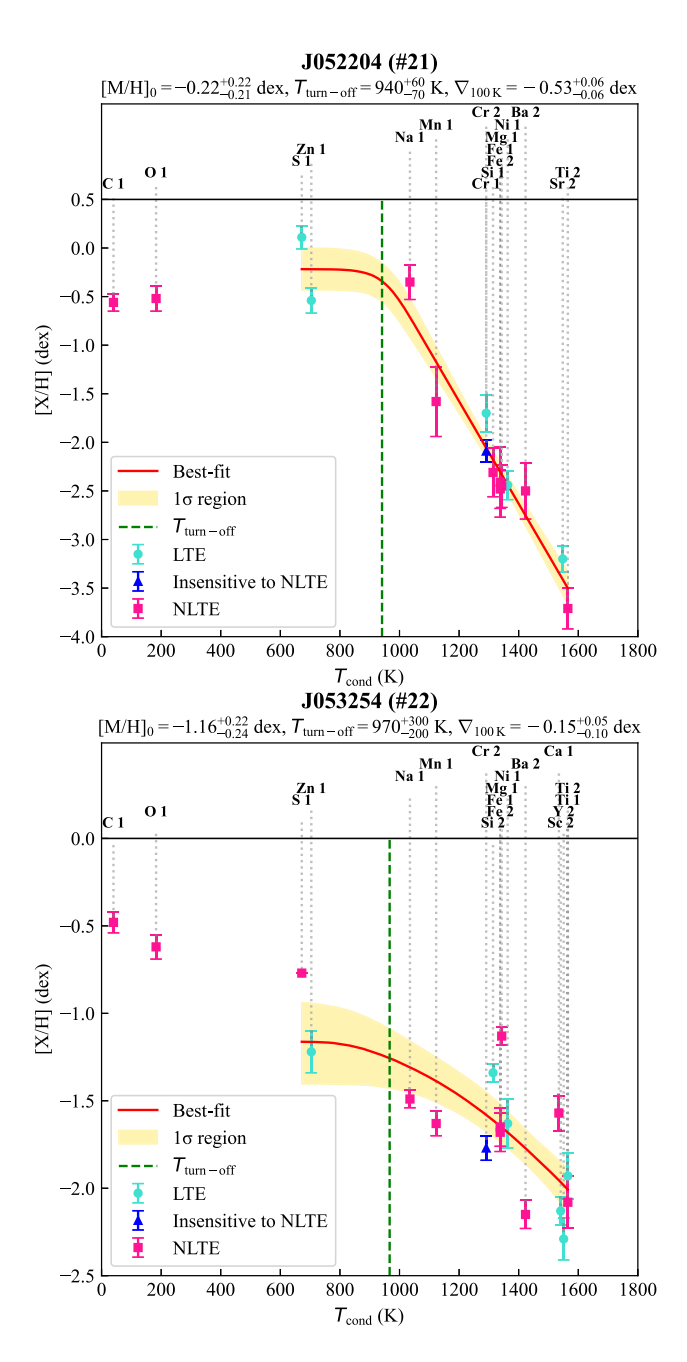


Figure 5. Elemental abundances of a subsample of post-AGB/post-RGB binaries with faint discs as functions of condensation temperature (Lodders 2003; Wood et al. 2019). For ID explanation, see Table 7. The legend for the symbols and colours used is included within the plot. 'NLTE insensitive' abundances are derived from spectral lines of V II and Cr II; for more details, see Section 3.2).

using half-normal distributions with a mean of 0 dex and a standard deviation of 10 dex. These weakly informative priors were chosen to reflect broad physical plausibility without enforcing strong constraints. Elemental abundances were treated as observational data with equal weighting across all fitted elements. Posterior predictions were obtained by sampling from the posterior distributions, and credible intervals were derived from the 16th and 84th percentiles.

Together, $[M/H]_0$, $T_{turn-off}$, and $\nabla_{100\,K}$ provide a simplified, yet comprehensive description of the observed depletion profiles in post-AGB and post-RGB binaries. In Figures 4 and 5, we present

Table 6. The references for model atoms used in this study (see Section 3.3).

Element	Reference
С	Amarsi et al. (2020)
N	Amarsi et al. (2020)
0	Amarsi et al. (2020)
Na	Amarsi et al. (2020)
Mg	Amarsi et al. (2020)
Al	Amarsi et al. (2020)
Si	Amarsi et al. (2020)
S	Amarsi et al. (2025)
K	Amarsi et al. (2020)
Ca	Amarsi et al. (2020)
Ti	Mallinson et al. (2024)
Mn	Amarsi et al. (2020)
Fe	Amarsi et al. (2022)
Cu	Caliskan et al. (2025)
Ва	Amarsi et al. (2020)

the depletion profile fits for faint disc targets (red solid lines) with corresponding 1σ -areas (yellow shaded regions). We note that CNO elements were excluded from the depletion fitting, as CNO surface abundances were significantly altered by nucleosynthetic and mixing processes during the AGB/RGB evolution, on scales comparable to and indiscernible from those of the depletion process (see Section 1).

We found that all derived NLTE depletion profiles of the faint disc targets show saturation (see Section 1). In Table 7, we list the adopted luminosities, atmospheric parameters, and depletion parameters of the faint disc targets. To further investigate depletion in faint disc targets, we examined how the derived depletion parameters vary with effective temperature, adopted luminosity, orbital period, and IR/stellar luminosity, as these parameters were shown to be moderately correlating with depletion in transition disc targets (Mohorian et al. 2025). Although we found a wide range of depletion parameters among faint disc targets, the small sample size prevented detection of any significant correlations or trends (see the distribution of faint disc targets in Figures 6, 7, 8, and 9). To build on these results, we extend our analysis to include full and transition disc targets, enabling a comparison of depletion profiles across different disc types.

4. Discussion

In this section, we examine the depletion characteristics of the faint disc targets and explore their broader implications for disc evolution. In Section 4.1, we compare faint disc systems to a previously analysed subset of post-AGB and post-RGB binaries hosting full and transition discs. In Section 4.2, we discuss how our findings inform current understanding of disc dissipation processes in these evolved binaries.

4.1 Depletion profiles across faint, full, and transition disc targets

To investigate how photospheric depletion varies across different evolutionary stages of post-AGB/post-RGB binaries, we extended

Table 7. Adopted luminosities and homogeneously derived atmospheric and depletion parameters (using E-iSpec and pySME; see Section 3) of the post-AGB/post-RGB binaries with faint, full, and transition discs. For more details, see Section 4.

ID	Name	$\log \frac{L_{\text{adopted}}}{L_{\odot}}$	$T_{ m eff}$ (K)	$\log g$ (dex)	[Fe/H] (dex)	$\xi_{\rm t}$ (km/s)	$[M/H]_0$ (dex)	$T_{\text{turn-off}}$ (K)	$ abla_{100\mathrm{K}}$ (dex)
Full d	lisc targets (Mohoi	rian et al. 2024)							
1	SZ Mon	2.58 ± 0.10	5460 ± 60	0.93 ± 0.10	-0.50 ± 0.05	4.37 ± 0.08	$-0.32^{+0.13}_{-0.11}$	1270^{+70}_{-90}	$-0.25^{+0.06}_{-0.07}$
2	DF Cyg	2.82 ± 0.07	5770 ± 70	1.92 ± 0.09	$+0.05\pm0.05$	3.97 ± 0.03	$+0.25^{+0.14}_{-0.12}$	1280^{+80}_{-80}	$-0.25^{+0.06}_{-0.08}$
Trans	sition disc targets (Mohorian et al. 20	025)						
3	CT Ori	3.26 ± 0.16	5940 ± 120	1.01 ± 0.18	-1.89 ± 0.11	3.37 ± 0.10	$-0.49^{+0.24}_{-0.25}$	840^{+140}_{-110}	$-0.24^{+0.04}_{-0.04}$
4	ST Pup	2.96 ± 0.17	5340 ± 80	0.20 ± 0.10	-1.92 ± 0.08	2.83 ± 0.03	$-0.67^{+0.19}_{-0.19}$	840^{+100}_{-100}	$-0.24^{+0.03}_{-0.03}$
5	RU Cen	3.50 ± 0.27	6120 ± 80	1.46 ± 0.15	-1.93 ± 0.08	3.26 ± 0.10	$-0.93^{+0.13}_{-0.14}$	750^{+100}_{-60}	$-0.14^{+0.02}_{-0.02}$
6	AC Her	3.71 ± 0.21	6140 ± 100	1.27 ± 0.16	-1.47 ± 0.08	3.92 ± 0.12	$-0.67^{+0.12}_{-0.13}$	850^{+120}_{-110}	$-0.15^{+0.02}_{-0.02}$
7	AD Aql	2.84 ± 0.29	6200 ± 170	1.67 ± 0.45	-2.20 ± 0.09	2.98 ± 0.36	$-0.07^{+0.20}_{-0.21}$	800^{+80}_{-80}	$-0.38^{+0.04}_{-0.05}$
8	EP Lyr	3.96 ± 0.23	6270 ± 160	1.24 ± 0.18	-2.03 ± 0.17	2.48 ± 0.10	$-0.65^{+0.16}_{-0.16}$	730^{+80}_{-40}	$-0.20^{+0.03}_{-0.03}$
9	DY Ori	3.50 ± 0.17	6160 ± 70	0.88 ± 0.14	-2.03 ± 0.04	2.48 ± 0.09	$+0.20^{+0.34}_{-0.33}$	890^{+120}_{-130}	$-0.38^{+0.07}_{-0.08}$
10	AF Crt	2.51 ± 0.17	6110 ± 110	0.96 ± 0.21	-2.47 ± 0.05	4.87 ± 0.16	$-0.34^{+0.36}_{-0.37}$	890^{+140}_{-130}	$-0.35^{+0.07}_{-0.08}$
11	GZ Nor	2.71 ± 0.29	5100 ± 80	0.49 ± 0.16	-1.65 ± 0.07	4.33 ± 0.05	$-0.89^{+0.14}_{-0.15}$	750^{+110}_{-50}	$-0.11^{+0.02}_{-0.02}$
12	V1504 Sco	3.71 ± 0.35	5980 ± 90	0.98 ± 0.17	-1.05 ± 0.07	4.29 ± 0.05	$+0.14^{+0.19}_{-0.17}$	950^{+70}_{-100}	$-0.31^{+0.05}_{-0.05}$
13	J050304	3.46 ± 0.20	5750 ± 100	0.00 ± 0.18	-2.61 ± 0.05	2.20 ± 0.01	$-0.77^{+0.33}_{-0.34}$	840^{+120}_{-110}	$-0.34^{+0.06}_{-0.07}$
14	J053150	3.99 ± 0.19	6160 ± 130	1.38 ± 0.20	-2.48 ± 0.04	4.28 ± 0.12	$-0.08^{+0.39}_{-0.34}$	960^{+80}_{-120}	$-0.42^{+0.08}_{-0.08}$
Faint	disc targets (this s	tudy)							
15	SS Gem	3.40 ± 0.20	6500 ± 90	1.96 ± 0.11	-1.02 ± 0.12	4.08 ± 0.09	$-0.33^{+0.12}_{-0.10}$	1030^{+80}_{-100}	$-0.17^{+0.03}_{-0.03}$
16	V382 Aur	3.35 ± 0.15	6020 ± 150	0.38 ± 0.27	-1.82 ± 0.08	4.14 ± 0.13	$-0.92^{+0.22}_{-0.24}$	820^{+170}_{-110}	$-0.14^{+0.04}_{-0.04}$
17	CC Lyr	2.99 ± 0.16	6470 ± 250	1.64 ± 0.50	-3.80 ± 0.03	4.14 ± 1.00	$-0.38^{+0.34}_{-0.36}$	860^{+100}_{-100}	$-0.51^{+0.07}_{-0.08}$
18	R Sct	3.10 ± 0.25	5630 ± 70	0.93 ± 0.11	-0.60 ± 0.11	2.93 ± 0.03	$-0.37^{+0.26}_{-0.20}$	1280^{+80}_{-110}	$-0.40^{+0.11}_{-0.12}$
19	AU Vul	3.82 ± 0.20	4740 ± 40	0.00 ± 0.09	-0.95 ± 0.08	4.32 ± 0.04	$-0.61^{+0.22}_{-0.20}$	1130^{+180}_{-240}	$-0.17^{+0.06}_{-0.10}$
20	BD+39 4926	3.79 ± 0.14	7470 ± 40	0.52 ± 0.05	-2.37 ± 0.18	2.21 ± 0.25	$+0.08^{+0.29}_{-0.31}$	850^{+130}_{-110}	$-0.44^{+0.08}_{-0.12}$
21	J052204	3.31 ± 0.11	7020 ± 100	1.65 ± 0.11	-2.49 ± 0.10	2.36 ± 0.04	$-0.22^{+0.21}_{-0.21}$	940^{+60}_{-70}	$-0.53^{+0.06}_{-0.06}$
22	J053254	3.84 ± 0.28	6040 ± 90	0.47 ± 0.13	-1.66 ± 0.09	2.36 ± 0.03	$-1.17^{+0.23}_{-0.24}$	970^{+300}_{-200}	$-0.15^{+0.05}_{-0.10}$

Notes: Post-AGB and post-RGB binaries are separated by the luminosity ($\log{(L/L_{\odot})} \gtrsim 3.4$ and $\log{(L/L_{\odot})} \lesssim 3.4$, respectively). Atmospheric parameters of GZ Nor (#11) were revised using a more conservative line list to decrease the line-to-line scatter of elemental abundances (see Table C.1).

our target sample by incorporating full and transition disc targets from Mohorian et al. (2024), (2025). We hereafter refer to this curated set of targets as the *combined sample*. Although we adopted the published LTE abundances and luminosities for these targets, we recalculated their NLTE corrections using pySME (as noted in Section 3.3), replacing the original Balder-based corrections used in the earlier studies (Mohorian et al. 2025). These revised corrections were then applied to the LTE abundances following the same procedure (see Section 3.3) used for the faint disc sample, ensuring a consistent framework across all targets. In Appendix E, we present the full details of recalculated abundances, applied NLTE corrections, and comparisons with previously published values. In Table 7, we summarise the adopted luminosities, atmospheric parameters, and derived depletion parameters of the combined sample.

To assess depletion efficiency across post-AGB/post-RGB binaries, we analysed how the depletion parameters (initial metallicity [M/H]₀, turn-off temperature $T_{\rm turn-off}$, and depletion scale $\nabla_{\rm 100\,K}$; see Section 3.4) vary across the combined sample of faint, full, and transition disc targets. Specifically, we explored trends with stellar effective temperature, bolometric luminosity, orbital period, and IR/stellar luminosity ratio (see Figures 6, 7, 8, and 9). These four parameters were selected based on the following considerations:

- Effective temperature ($T_{\rm eff}$) can serve as a proxy for evolutionary stage along the post-AGB/post-RGB track (Oomen et al. 2019; Martin et al. 2025). Although $T_{\rm eff}$ is not a perfect indicator since accretion is known to stall the evolution of post-AGB/post-RGB stars it remains informative. Martin et al. (2025) showed that with accretion rates up to 10^{-6} M $_{\odot}$ /yr and disc masses up to 3×10^{-2} M $_{\odot}$, the post-AGB/post-RGB phase may be extended by up to a factor of 10. Despite this, $T_{\rm eff}$ still provides a reasonable baseline for assessing whether a target is in an earlier or later stage of post-AGB/post-RGB evolution.
- Bolometric luminosity offers a means of distinguishing between more luminous post-AGB stars and less luminous post-RGB stars, with an approximate boundary at $L \sim 2\,500\,{\rm L}_{\odot}$ (log $\frac{L}{L_{\odot}} \sim 3.4$), depending on the metallicity (Kamath et al. 2016).
- Orbital period is an important tracer of binary interaction history (van Winckel 2003, 2018; Oomen et al. 2020).
 However, this parameter is only available for only 10 of the 18 Galactic targets in our sample, limiting its statistical robustness and making it susceptible to small-number statistics and observational biases.

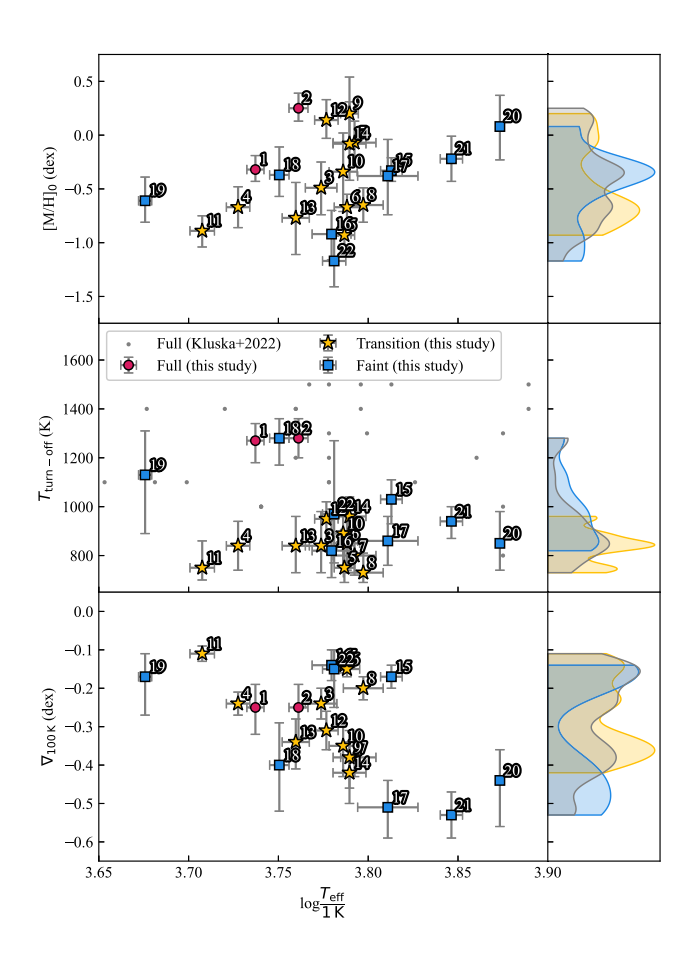


Figure 6. Distributions of depletion pattern parameters with effective temperature as a proxy for age on post-AGB/post-RGB track ($upper\,panel$: initial metallicity [M/H]₀, $middle\,panel$: $T_{turn-off}$, $lower\,panel$: depletion gradient $\nabla_{100\,K}$). For target ID specification, see Table 7. Red circles represent full disc targets, yellow stars represent transition disc targets, blue squares represent faint disc targets. Grey dots in $T_{turn-off}$ subplot represent the Galactic full disc targets with visually estimated values of $T_{turn-off}$ (Kluska et al. 2022). Small right panels display the distributions of depletion parameters within the targets hosting transition discs (yellow), faint discs (blue), and all types of discs (gray). For more details on depletion pattern parameters, see Section 4.

The IR/stellar luminosity ratio (L_{IR}/L_{*}) serves as a proxy for the disc mass or optical thickness (de Ruyter et al. 2006). However, this quantity is affected by disc geometry. Disentangling this effect requires radiative transfer modelling constrained by spatially resolved observations, which lies beyond the scope of this study.

The main findings from our comparison of the NLTE-corrected depletion profiles across the combined sample are summarised below:

- The initial metallicity [M/H]₀ shows significant target-totarget variability with no overarching trend, suggesting that the depletion process operates independently of initial metallicity.
- The $T_{\rm turn-off}$ values differ between disc types: both full disc post-RGB systems (SZ Mon, #1; and DF Cyg, #2) show $T_{\rm turn-off} \sim 1\,300$ K, while transition disc targets (both post-RGB and post-AGB) exhibit $T_{\rm turn-off} \sim 900$ K (see Figures 6, 7, 8, and 9). This morphological difference suggests distinct disc-formation mechanisms. Based on this,

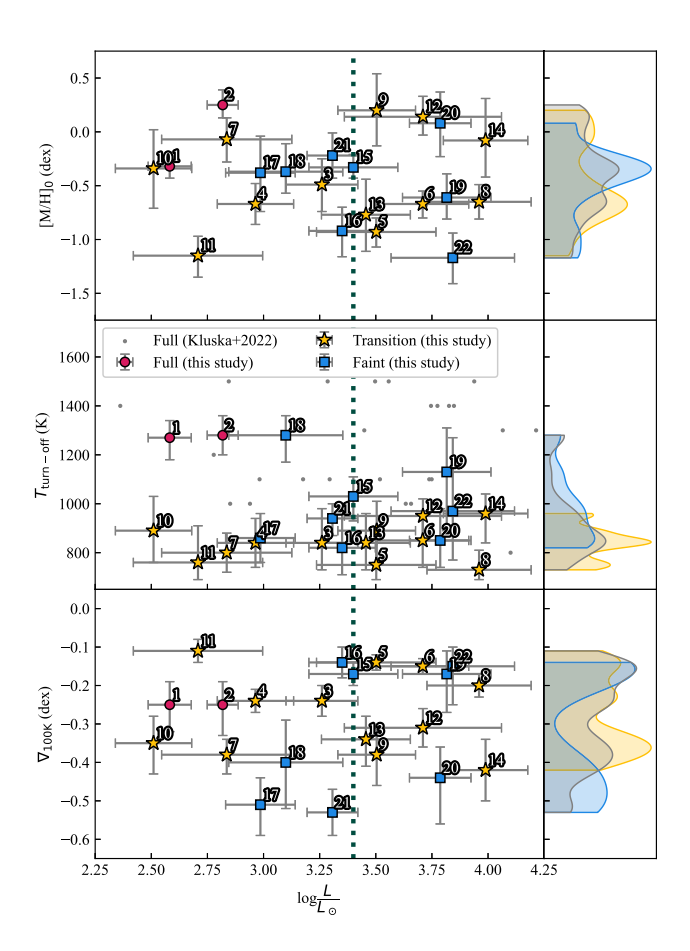


Figure 7. Distributions of depletion pattern parameters with adopted luminosity (upper panel: initial metallicity [M/H] $_0$, middle panel: $T_{\rm turn-off}$, lower panel: depletion gradient $\nabla_{100\,\rm K}$). For target ID specification, see Table 7. Red circles represent full disc targets, yellow stars represent transition disc targets, blue squares represent faint disc targets. Vertical dotted line represents rough demarcation between post-AGB and post-RGB binaries ($L\sim2\,500\,\rm L_\odot$; $\log\frac{L}{L_\odot}\sim3.4$). Grey dots in $T_{\rm turn-off}$ subplot represent the Galactic full disc targets with visually estimated values of $T_{\rm turn-off}$ (Kluska et al. 2022). Small right panels display the distributions of depletion parameters within the targets hosting transition discs (yellow), faint discs (blue), and all types of discs (gray). For more details on depletion pattern parameters, see Section 4.

we classified faint disc targets into two subgroups: (i) full-like disc targets with $T_{\rm turn\text{-}off} > 1\,100$ K (R Sct, #18; and AU Vul, #19) and (ii) transition-like disc targets with $T_{\rm turn\text{-}off} < 1\,100$ K (SS Gem, #15; V382 Aur, #16; CC Lyr, #17; BD+39 4926, #20; J052204, #21; and J053254, #22). In future studies, we will explore this classification further through homogeneous chemical analysis of full disc targets in the Galaxy and in the LMC.

• The depletion scale $\nabla_{100\,\mathrm{K}}$ shows a bimodal distribution among faint disc targets and a more stochastic distribution across the combined sample. Three high- T_{eff} faint disc targets (AU Vul, #19; BD+39 4926, #20; J052204, #21) contribute strongly to the bimodality, showing steep depletion gradients ($\nabla_{100\,\mathrm{K}} < -0.4$ dex; see lower right panel of Figures 6, 7, 8, and 9). The overall stochasticity of $\nabla_{100\,\mathrm{K}}$ is consistent with the established picture of chemical depletion, in which refractory elements are rapidly sequestered into dust and prevented from re-accretion, potentially erasing earlier RGB/AGB nucleosynthetic signatures.

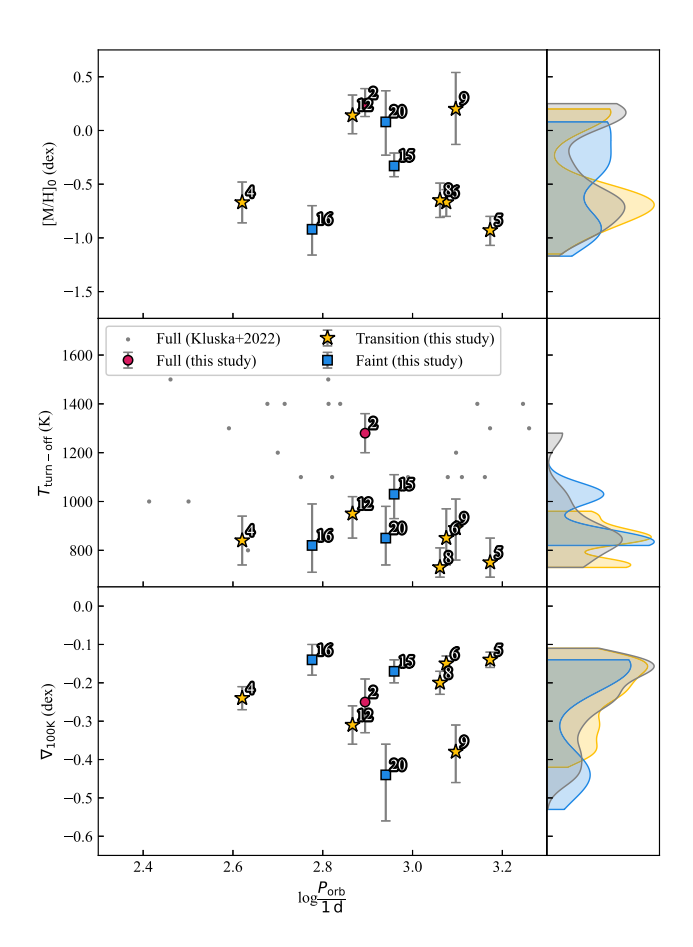


Figure 8. Distributions of depletion pattern parameters with orbital period (upper panel: initial metallicity $[M/H]_o$, middle panel: $T_{turn-off}$, lower panel: depletion gradient $\nabla_{100\,\text{K}}$). For target ID specification, see Table 7. Red circles represent full disc targets, yellow stars represent transition disc targets, blue squares represent faint disc targets. Grey dots in $T_{\text{turn-off}}$ subplot represent the Galactic full disc targets with visually estimated values of $T_{\text{turn-off}}$ (Kluska et al. 2022). Small right panels display the distributions of depletion parameters within the targets hosting transition discs (yellow), faint discs (blue), and all types of discs (gray). For more details on depletion pattern parameters, see Section 4.

- Depletion is notably more efficient in post-AGB/post-RGB binaries than in Sun-like planet hosts. The average depletion scale is $\nabla_{100\,\mathrm{K}} \sim -0.3$ dex in our sample, compared to $\nabla_{100\,\mathrm{K}} \sim -0.01$ dex in young planet-hosting stars (Yun et al. 2024). This efficiency likely reflects more effective gas-dust fractionation in CBDs or smaller convective envelopes ($\sim 10^{-3}$ – 10^{-2} M_{\odot}) that retain chemical imprints more easily (Oomen et al. 2020).
- Four LMC targets (J050304, #13; J053150, #14; J052204, #21; J053254, #22) follow the same depletion trends as Galactic systems, suggesting that initial metallicity has little influence on depletion efficiency.
- Transition disc target EP Lyr (#8) with a wide inner gap (based on mid-IR interferometry; Corporaal et al. 2023), has a low IR/stellar luminosity ratio ($L_{\rm IR}/L_*=0.02$) that belongs within the range for faint discs ($0 < L_{\rm IR}/L_* < 0.1$). This suggests a potential evolutionary connection between faint and transition disc systems.
- In Figure 9, the $L_{\rm IR}/L_*$ - $T_{\rm turn-off}$ subplot (middle panel) allows for segregation of full, transition, and faint disc targets. This further supports the idea that disc types might

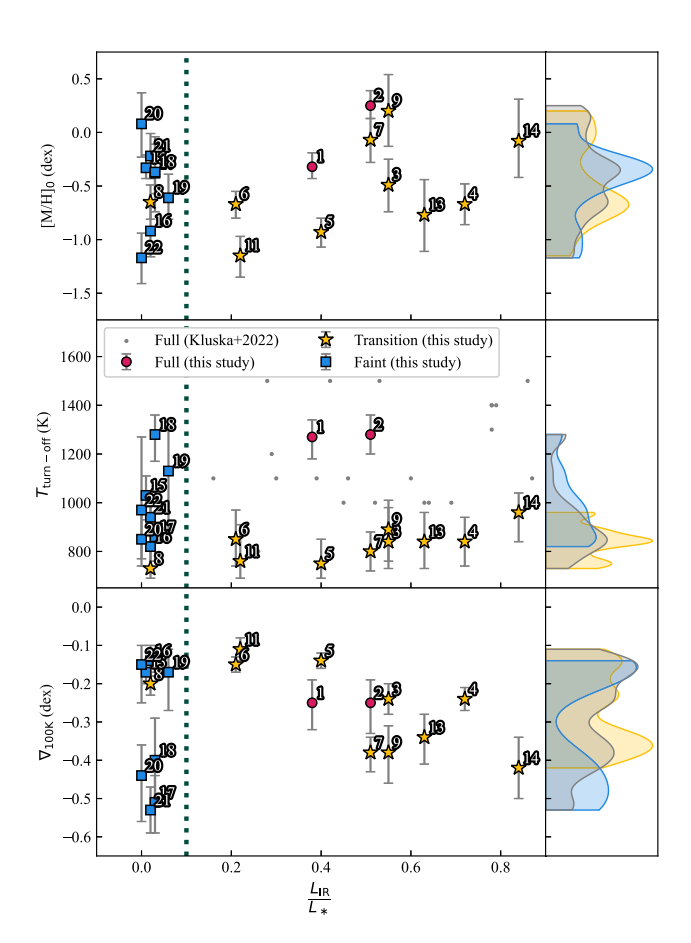


Figure 9. Distributions of depletion pattern parameters with IR/stellar luminosity ratio (upper panel: initial metallicity $[\rm M/H]_{o}$, middle panel: $T_{\rm turn-off}$, lower panel: depletion gradient $V_{\rm 100\,K}$). Targets with $L_{\rm IR}/L_* > 0.9$ are excluded from the figure because these systems are viewed at high inclinations (i.e. close to edge-on). In such cases, the observed IR excess is strongly affected by geometric effects, requiring a more careful and detailed interpretation before meaningful conclusions can be drawn. For target ID specification, see Table 7. Red circles represent full disc targets, yellow stars represent transition disc targets, blue squares represent faint disc targets. Vertical dotted line represents rough demarcation between faint and full/transition disc targets with visually estimated values of $T_{\rm turn-off}$ (Kluska et al. 2022). Small right panels display the distributions of depletion parameters within the targets hosting transition discs (yellow), faint discs (blue), and all types of discs (gray). For more details on depletion pattern parameters, see Section 4.

reflect different evolutionary stages. To validate this, we plan to expand our abundance analyses to full disc systems in the Galaxy and Magellanic Clouds (Kluska et al. 2022; Kamath et al. 2014; Kamath et al. 2015).

• In Figure 9, the $L_{\rm IR}/L_*$ - $\nabla_{100\,\rm K}$ subplot (lower panel) shows that transition disc targets with higher $L_{\rm IR}/L_*$ tend to exhibit steeper depletion slopes ($\nabla_{100\,\rm K}$), with a statistically significant Spearman correlation ($\rho_s = -0.70$). However, this trend may be affected by system inclination and dust mass, which are difficult to disentangle without full orbital solutions (available for only 6 of 12 transition disc targets). As depletion scale is also shaped by disc evolution, further study is needed to interpret this correlation robustly.

Finally, although our results do not reveal a clear relation between stellar and depletion parameters, understanding the underlying physical and chemical mechanisms remains crucial.

In particular, interpretation of the observed depletion parameter distributions requires developing detailed models of individual CBDs (including processes of dust condensation, inward transport, and gas-dust decoupling). To gain deeper insight into photospheric depletion observed in post-AGB/post-RGB binaries, our future work will focus on advancing the modelling of the depletion process through re-accretion, building on the initial works of Oomen et al. (2019, 2020), Martin et al. (2025). This will involve incorporating more sophisticated disc physics, including photo-evaporation, binary-induced torques, irradiation from central binary, and spatial or temporal variations in the chemical composition of re-accreted material.

4.2 Disc dissipation around post-AGB and post-RGB binaries

Post-AGB and post-RGB binary stars were traditionally identified by the significant IR excesses in their SEDs (see Section 1). However, faint disc targets with low IR excesses (\sim 10% of post-AGB/post-RGB binary sample in the Galaxy; Kluska et al. 2022) still show clear signs of photospheric depletion (see Table 2). This suggests that these faint disc systems likely hosted full or transition discs during an earlier phase of disc-binary interaction. Our findings support this interpretation and strengthen the categorisation of faint disc systems into full-like and transition-like subsets (see Section 4.1).

Although the faint disc sample is not systematically hotter (i.e. more evolved; see Section 4.1) than the full or transition disc samples, 7 of 8 faint disc targets - SS Gem (#15), V382 Aur (#16), CC Lyr (#17), R Sct (#18), BD+39 4926 (#20), J052204 (#21), and J053254 (#22) - have moderate-to-high effective temperatures ($T_{\rm eff} > 5\,500$ K). These targets might represent the progeny of full or transition disc targets that since dissipated, potentially through a combination of grain growth, radial drift, and photo-evaporation (as proposed for young stars with dissipated protoplanetary discs; see Alexander, Clarke, & Pringle 2006; Alexander et al. 2014, and references therein). This hypothesis is plausible given reported jet-driven mass-loss rates of 10⁻⁸-10⁻⁶ M_☉/yr in post-AGB/post-RGB systems (Bollen et al. 2022; Verhamme et al. 2024). Recently, De Prins et al. (2024) presented the first MHD models of such jets, reporting higher mass-loss rates $(10^{-6}-10^{-3} \text{ M}_{\odot}/\text{yr})$, though they noted these values are likely overestimated for post-AGB/post-RGB binaries. Even under conservative assumptions, a post-AGB/post-RGB system could lose \sim $10^{-3}~{\rm M}_{\odot}$ of CBD material over the $\sim 10^5$ -yr duration of the post-AGB phase (Miller Bertolami 2016). This is a significant fraction of the total disc mass typically observed in post-AGB/post-RGB binaries ($M_{\rm disc} \lesssim 10^{-2} \, \rm M_{\odot}$; see Table 4.7 in Gallardo Cava 2023). Confirming this dissipation scenario will require direct analysis of the gas and dust distribution in faint discs using interferometric facilities, including Atacama Large Millimeter/submillimeter Array (ALMA) and Very Large Telescope Interferometer (VLTI).

In addition, the disc dissipation hypothesis is further supported by the case of BD+15 2862 (see Section 2.1), a target with extremely low IR excess ($L_{\rm IR}/L_* < 0.01$) and a wide orbit ($P_{\rm orb} = 530.9$ d). Although excluded from our depletion analysis due to its high effective temperature ($T_{\rm eff} \sim 12\,000$ K; see Section 2.1), which precludes a homogeneous Fe line analysis with E-iSpec, BD+15 2862 is known to be extremely depleted, with abundances determined for only seven elements, including [S/H] = -0.1 dex and [Fe/H] < -3 dex (Giridhar & Arellano Ferro 2005). This system likely represents an advanced evolutionary stage along

the post-AGB/post-RGB track, illustrating severe photospheric depletion in the final stages of CBD evolution.

We note that the faint disc target AU Vul (#19) is an outlier in the disc dissipation scenario. This post-AGB binary is the coolest target in our combined sample ($L \sim 6\,550\,\mathrm{L}_{\odot}$, $T_{\rm eff} =$ 4740 ± 40 K; see, e.g. Kluska et al. 2022). Although $T_{\rm eff}$ is not a perfect indicator of post-AGB age (due to potential stalling by accretion; see Section 4.1), it is reasonable to infer that AU Vul (#19) spent less time on the post-AGB track than other faint disc targets. Nevertheless, this target exhibits a significant depletion slope ($\nabla_{100 \, \text{K}} = -0.17^{+0.06}_{-0.10}$ dex), suggesting that disc dissipation and/or dust settling occurred unusually early or rapidly, possibly due to binary interaction, low initial disc mass, or an alternative dispersal mechanism. To better understand depletion in cool, chemically depleted post-AGB/post-RGB binaries, further homogeneous chemical analysis of similarly cool full disc targets are required. In addition, a homogeneous chemical analysis of all full disc targets in the Galaxy and the Magellanic Clouds will allow a robust test of our assumption that $T_{turn-off}$ can serve as a discriminant between full and transition disc systems.

More generally, several physical mechanisms could accelerate disc dissipation and/or dust settling in post-AGB/post-RGB systems – one possible contributor is planet formation. The growth of pebbles and planetesimals can generate additional pressure bumps that efficiently trap dust within the disc (Eriksson, Johansen, & Liu 2020; Shibaike & Alibert 2023; Drażkowska et al. 2023; Price, Van Clepper, & Ciesla 2025). The IR excesses in the SEDs of faint disc targets (see Figure 3) suggest that, if disc asymmetries or planet-induced spiral structures exist, they could be detectable with current interferometric facilities (e.g. ALMA and VLTI). Observing disc asymmetries in full, transition, and faint disc targets would provide critical insights into the role of planet formation in driving and modifying disc dissipation and dust-settling processes (Hillen et al. 2017; Kluska et al. 2018, 2019; Andrych et al. 2023; Andrych et al. 2024).

To interpret this possibility, and to understand why faint and transition discs remain relatively rare among the post-AGB/post-RGB sample, current planet formation models for protoplanetary discs around young stars (see, e.g. Raymond & Morbidelli 2022, and references therein) need to be adapted to the unique conditions of CBDs around post-AGB/post-RGB binaries. This includes accounting for stellar irradiation, gas-to-dust ratios, and both chemical and spatial disc structures. Our ongoing observational and theoretical work will continue to investigate the evolution and mechanisms of photospheric depletion in these systems.

5. Conclusions

The aim of this study was to investigate the link between CBD evolution and photospheric depletion in post-AGB/post-RGB binaries with faint discs. For this aim, we performed a detailed chemical abundance analysis based on high-resolution optical spectra obtained with HERMES/Mercator and UVES/VLT. Using the E-iSpec code, we derived precise atmospheric parameters and elemental abundances for eight post-AGB/post-RGB binaries with faint discs in both the Galaxy and the LMC. In addition, we employed pySME to compute NLTE corrections for individual lines of a representative set of chemical elements from carbon to barium.

To consistently analyse the depletion profiles of faint disc targets, we fitted each profile with a two-piece linear function defined by three free parameters: initial metallicity [M/H] $_0$, turn-off temperature $T_{\rm turn-off}$, and depletion scale $\nabla_{100\,\rm K}$. Our analysis of NLTE-corrected depletion profiles of faint disc targets revealed that these profiles are 'saturated', with a weak bimodality in the $T_{\rm turn-off}$ distribution centered around $\sim\!900$ and $\sim\!1$ 300 K, and a strong bimodality in the $\nabla_{100\,\rm K}$ distribution clustered near $\sim\!-0.45$ and $\sim\!-0.15$ dex (see blue distributions in the right panels of Figures 6, 7, 8, and 9). Overall, [M/H] $_0$ spans from -1.17 to +0.25 dex, $T_{\rm turn-off}$ ranges from 730 to 1 280 K, and $\nabla_{100\,\rm K}$ extends from -0.53 to -0.11 dex.

To place our results in context, we combined our faint disc sample with a previously studied subset of post-AGB/post-RGB binaries hosting full and transition discs. The distributions of $[M/H]_0$ and $\nabla_{100\,K}$ in the combined sample of post-AGB/post-RGB binaries appear stochastic, whereas the distribution of $T_{\text{turn-off}}$ shows two distinct peaks at ~ 900 and ~ 1300 K. Based on this bimodality, we categorised the faint disc sample into two subgroups: (i) full-like targets and (ii) transition-like targets. This categorisation suggests that different disc formation and evolution mechanisms may underlie the morphological differences in depletion profiles between the full and transition disc targets. The precise location of dust-gas separation within the disc, and its overlap with the disc region re-accreted onto the star, remain open questions. We note that our sample size is limited, and the observed trends may be affected by small-number statistics and selection biases. This work will be extended by our ongoing homogeneous abundance analysis of post-AGB/post-RGB binaries with full discs in the Galaxy and the Magellanic Clouds.

Our results confirm that post-AGB and post-RGB binaries with faint discs, despite their low IR excesses, retain strong photospheric depletion signatures, indicating that these systems previously hosted full or transition discs. Most faint disc targets (7 of 8) likely represent the final evolutionary stages of circumbinary disc dissipation, analogous to photoevaporation-driven clearing in protoplanetary systems. The cool faint disc target AU Vul (#19) is an outlier, showing significant depletion despite being relatively less evolved, suggesting unusually rapid disc dissipation and/or dust settling. In our combined sample, we also find a significant anticorrelation between IR-to-stellar luminosity ratio and depletion slope in transition disc systems.

These findings highlight the need to investigate the gas and dust distribution in CBDs by combining homogeneous abundance analyses of full, transition, and faint disc targets with high-resolution imaging and detailed physical—chemical modelling. The diversity of depletion profiles across these disc types underscores the complexity of disc—binary interactions in post-AGB/post-RGB binaries. To better constrain the processes driving photospheric depletion, we are expanding both our sample and methodological approach — an essential step towards understanding the full diversity of depletion profiles in the post-AGB/post-RGB binary population.

Acknowledgements. The spectroscopic results presented in this study are based on observations obtained with the HERMES spectrograph, which is supported by the Research Foundation - Flanders (FWO), Belgium, the Research Council of KU Leuven, Belgium, the Fonds National de la Recherche Scientifique (F.R.S.-FNRS), Belgium, the Royal Observatory of Belgium, the Observatoire de Genève, Switzerland and the Thüringer Landessternwarte Tautenburg, Germany. This research is also based on observations collected at the European Organisation for Astronomical Research in the Southern Hemisphere under ESO programmes 074.D-0619 and 092.D-0485. This

research was supported by computational resources provided by the Australian Government through the National Computational Infrastructure (NCI) under the National Computational Merit Allocation Scheme and the ANU Merit Allocation Scheme (project y89).

MM1 acknowledges the International Macquarie Research Excellence Scholarship program (iMQRES) for financial support during the research. MM1, DK, HVW, and KA acknowledge the support of the Australian Research Council Discovery Project DP240101150. AMA acknowledges support from the Swedish Research Council (VR 2020-03940), the Crafoord Foundation via the Royal Swedish Academy of Sciences (CR 2024-0015), and the European Union's Horizon Europe research and innovation programme under grant agreement No. 101079231 (EXOHOST).

Data availability statement. The data underlying this article are available in the article and in its online supplementary material.

```
References
Agúndez, M., Martnez, J. I., de Andres, P. L., Cernicharo, J., & Martn-Gago, J.
   A. 2020, A&A, 637, A59
Alcolea, J., et al. 2023, arXiv e-prints, arXiv:2311.16734
Alexander, R., Pascucci, I., Andrews, S., Armitage, P., & Cieza, L. 2014, in
   Protostars and Planets VI, ed. H. Beuther, R. S. Klessen, C. P. Dullemond, &
Alexander, R. D., Clarke, C. J., & Pringle, J. E. 2006, MNRAS, 369, 229
Amarsi, A., Li, W., Grevesse, N., & Jurewicz, A. 2025, submitted to A&A, 11
Amarsi, A. M., Liljegren, S., & Nissen, P. E. 2022, A&A, 668, A68
Amarsi, A. M., et al. 2018, A&A, 615, A139
Amarsi, A. M., et al. 2020, A&A, 642, A62
Andrievsky, S. M., et al. 2002, A&A, 396, 641
Andrych, K., et al. 2023, MNRAS, 524, 4168
Andrych, K., et al. 2024, MNRAS, 535, 1763
Asplund, M., Amarsi, A. M., & Grevesse, N. 2021, A&A, 653, A141
Bailer-Jones, C. A. L., Rybizki, J., Fouesneau, M., Demleitner, M., & Andrae, R.
   2021, AJ, 161, 147
Blanco-Cuaresma, S. 2019, MNRAS, 486, 2075
Blanco-Cuaresma, S., Soubiran, C., Heiter, U., & Jofré, P. 2014, A&A,
   569, A111
Bollen, D., et al. 2022, A&A, 666, A40
Bujarrabal, V., Castro-Carrizo, A., Alcolea, J., & Van Winckel, H. 2015, A&A,
Bujarrabal, V., et al. 2018, A&A, 614, A58
Caliskan, S., et al. 2025, A&A, 696, A210
Cardelli, J. A., Clayton, G. C., & Mathis, J. S. 1989, ApJ, 345, 245
Castelli, F., & Kurucz, R. L. 2003, in 210th Symposium of the International
   Astronomical Union held at Uppsala University, Vol. 210, Modelling of
   Stellar Atmospheres, ed. N. Piskunov, W. W. Weiss, & D. F. Gray, A20
Corporaal, A., et al. 2023, A&A, 674, A151
```

Cousins, A. W. J. 1976, MNSSA, 35, 70 Cutri, R. M., et al. 2012, VizieR Online Data Catalog: 2MASS 6X Point Source Working Database/Catalog (Cutri+ 2006), VizieR On-line Data Catalog: II/281. Originally published in: 2012yCat.2281...0C

Cutri, R. M., et al. 2021, VizieR Online Data Catalog: AllWISE Data Release (Cutri+ 2013), VizieR On-line Data Catalog: II/328. Originally published in: IPAC/Caltech (2013)

De Prins, T., et al. 2024, A&A, 689, A151

de Ruyter, S., van Winckel, H., Dominik, C., Waters, L. B. F. M., & Dejonghe, H. 2005, A&A, 435, 161

de Ruyter, S., et al. 2006, A&A, 448, 641

Degroote, P., et al. 2013, in EAS Publications Series, Vol. 64, EAS Publications Series, ed. K. Pavlovski, A. Tkachenko, & G. Torres, 277

Dekker, H., D'Odorico, S., Kaufer, A., Delabre, B., & Kotzlowski, H. 2000, in Society of Photo-Optical Instrumentation Engineers (SPIE) Conference Series, Vol. 4008, Optical and IR Telescope Instrumentation and Detectors, ed. M. Iye & A. F. Moorwood, 534

```
Dell'Agli, F., et al. 2023, A&A, 671, A86
Drażkowska, J., et al. 2023, in Astronomical Society of the Pacific Conference
   Series, Vol. 534, Protostars and Planets VII, ed. S. Inutsuka, Y. Aikawa, T.
  Muto, K. Tomida, & M. Tamura, 717
Eriksson, L. E. J., Johansen, A., & Liu, B. 2020, A&A, 635, A110
Ertel, S., et al. 2019, AJ, 157, 110
Flower, P. J. 1996, ApJ, 469, 355
Gallardo Cava, I. 2023, arXiv e-prints, arXiv:2311.08034
Gallardo Cava, I., Alcolea, J., Bujarrabal, V., Gómez-Garrido, M., & Castro-
  Carrizo, A. 2023, A&A, 671, A80
Gallardo Cava, I., et al. 2021, A&A, 648, A930
Gezer, I., et al. 2015, MNRAS, 453, 133
Gielen, C., et al. 2009, A&A, 508, 1391
Gielen, C., Cami, J., Bouwman, J., Peeters, E., & Min, M. 2011a, A&A, 536, A54
Gielen, C., et al. 2011b, A&A, 533, A99
Giridhar, S., & Arellano Ferro, A. 2005, A&A, 443, 297
Giridhar, S., Lambert, D. L., & Gonzalez, G. 2000, ApJ, 531, 521
Giridhar, S., Lambert, D. L., Reddy, B. E., Gonzalez, G., & Yong, D. 2005, ApJ,
Gonzalez, G., Lambert, D. L., & Giridhar, S. 1997, ApJ, 481, 452
Gorlova, N., et al. 2011, in Asymmetric Planetary Nebulae 5 Conference, ed. A.
  A. Zijlstra, F. Lykou, I. McDonald, & E. Lagadec, 246
Gorlova, N., et al. 2012, A&A, 542, A27
Griffin, M. J., et al. 2010, A&A, 518, L3
Gustafsson, B., et al. 2008, A&A, 486, 951
Heath, R. M., & Nixon, C. J. 2020, A&A, 641, A64
Hillen, M., et al. 2015, A&A, 578, A40
Hillen, M., et al. 2017, A&A, 599, A41
Hillen, M., et al. 2016, A&A, 588, L1
Høg, E., et al. 2000, A&A, 355, L27
Hrivnak, B. J., et al. 2008, AJ, 136, 1557
Ishihara, D., et al. 2010, A&A, 514, A1
Jermyn, A. S., & Kama, M. 2018, MNRAS, 476, 4418
Johnson, H. L., & Morgan, W. W. 1953, ApJ, 117, 313
Jura, M. 2015, AJ, 150, 166
Kalaee, M. J., & Hasanzadeh, A. 2019, New A, 70, 57
Kama, M., Folsom, C. P., & Pinilla, P. 2015, A&A, 582, L10
Kamath, D., et al. 2023, MNRAS, 519, 2169
Kamath, D., Wood, P. R., & Van Winckel, H. 2014, MNRAS, 439, 2211
Kamath, D., Wood, P. R., & Van Winckel, H. 2015, MNRAS, 454, 1468
Kamath, D., Wood, P. R., Van Winckel, H., & Nie, J. D. 2016, A&A,
  586, L5
Kiss, L. L., & Bódi, A. 2017, A&A, 608, A99
Kluska, J., et al. 2018, A&A, 616, A153
Kluska, J., et al. 2022, A&A, 658, A36
Kluska, J., et al. 2019, A&A, 631, A108
Kobayashi, C., Karakas, A. I., & Lugaro, M. 2020, ApJ, 900, 179
Kupka, F., Dubernet, M. L., & VAMDC COLLABORATION. 2011, BaltA, 20, 503
Lafler, J., & Kinman, T. D. 1965, ApJS, 11, 216
Lind, K., & Amarsi, A. M. 2024, arXiv e-prints, arXiv:2401.00697
Lodders, K. 2003, ApJ, 591, 1220
Lomb, N. R. 1976, Ap&SS, 39, 447
Maas, T., Giridhar, S., & Lambert, D. L. 2007, ApJ, 666, 378
Maas, T., Van Winckel, H., & Lloyd Evans, T. 2005, A&A, 429, 297
Mallinson, J. W. E., Lind, K., Amarsi, A. M., & Youakim, K. 2024, A&A,
  687, A5
Manick, R., Van Winckel, H., Kamath, D., Sekaran, S., & Kolenberg, K. 2018,
  A&A, 618, A21
Martin, K., De Marco, O., Kamath, D., Oomen, G.-M., & Van Winckel, H. 2025,
  arXiv e-prints, arXiv:2502.04660
Menon, M., Kamath, D., Mohorian, M., Van Winckel, H., & Ventura, P. 2024,
  PASA, 41, e025
Miller Bertolami, M. M. 2016, A&A, 588, A25
Mohorian, M., et al. 2025, arXiv e-prints, arXiv:2502.21043
Mohorian, M., et al. 2024, MNRAS, 530, 761
Murphy, S. J., et al. 2020, MNRAS, 499, 2701
Neugebauer, G., et al. 1984, ApJ, 278, L1
```

```
642, A234
Oomen, G.-M., Van Winckel, H., Pols, O., & Nelemans, G. 2019, A&A,
   629, A49
Oomen, G.-M., et al. 2018, A&A, 620, A85
Paczyński, B. 1971, ARA&A, 9, 183
Pawlak, M., et al. 2019, MNRAS, 487, 5932
Penzlin, A. B. T., Kley, W., Audiffren, H., & Schäfer, C. M. 2022, A&A,
  660, A101
Poglitsch, A., et al. 2010, A&A, 518, L2
Price, E. M., Van Clepper, E., & Ciesla, F. J. 2025, ApJ, 979, 37
Rao, S. S., Giridhar, S., & Lambert, D. L. 2012, MNRAS, 419, 1254
Raskin, G., et al. 2011, A&A, 526, A69
Raymond, S. N., & Morbidelli, A. 2022, in Astrophysics and Space Science
  Library, Vol. 466, Demographics of Exoplanetary Systems, Lecture Notes of
   the 3rd Advanced School on Exoplanetary Science, ed. K. Biazzo, V. Bozza,
  L. Mancini, & A. Sozzetti, 3
Reyniers, M., et al. 2007, A&A, 461, 641
Scargle, J. D. 1982, ApJ, 263, 835
Scicluna, P., et al. 2020, MNRAS, 494, 2925
Shibaike, Y., & Alibert, Y. 2023, A&A, 678, A102
Skrutskie, M. F., et al. 2006, AJ, 131, 1163
Sneden, C., Bean, J., Ivans, I., Lucatello, S., & Sobeck, J. 2012, MOOG: LTE line
  analysis and spectrum synthesis, Astrophysics Source Code Library, record
Soszyński, I., et al. 2008, Acta Astron., 58, 293
Thompson, G. I., et al. 1978, Catalogue of stellar ultraviolet fluxes: a compila-
  tion of absolute stellar fluxes measured by the Sky Survey Telescope (S2/68)
  aboard the ESRO satellite TD-1/(LCCN: 79-310488 (BKS3))
Torres, G. 2010, AJ, 140, 1158
Tosi, S., et al. 2022, A&A, 668, A22
Van Winckel, H. 1997, A&A, 319, 561
van Winckel, H. 2003, ARA&A, 41, 391
Van Winckel, H. 2018, arXiv e-prints, arXiv:1809.00871
Van Winckel, H., Mathis, J. S., & Waelkens, C. 1992, Natur, 356, 500
Van Winckel, H., Waelkens, C., & Waters, L. B. F. M. 1995, A&A, 293, L25
van Winckel, H., et al. 2009, A&A, 505, 1221
Venn, K. A., & Lambert, D. L. 1990, ApJ, 363, 234
Verhamme, O., et al. 2024, A&A, 684, A79
Waelkens, C., Van Winckel, H., Bogaert, E., & Trams, N. R. 1991, A&A,
   251, 495
Wehrhahn, A., Piskunov, N., & Ryabchikova, T. 2023, A&A, 671, A171
Wood, B. J., Smythe, D. J., & Harrison, T. 2019, AM, 104, 844
Woods, P. M., et al. 2011, MNRAS, 411, 1597
Wright, E. L., et al. 2010, AJ, 140, 1868
York, D. G., et al. 2000, AJ, 120, 1579
Yun, S., et al. 2024, ApJ, 971, 35
Zong, W., et al. 2020, ApJS, 251, 15
```

Oomen, G.-M., Pols, O., Van Winckel, H., & Nelemans, G. 2020, A&A,

Appendix A. Additional notes on selected targets

In this Appendix, we provide supplementary information on the circumstellar gas and dust characteristics of several targets, based on previous studies not included in Table 2. Specifically, we include additional notes for SS Gem, V382 Aur, R Sct, and BD+39

SS Gem. The RV phase curve of this target displays a long-term modulation of the mean brightness, superimposed on regular pulsations, known as RVb phenomenon (see Table 2). This additional variability is attributed to binarity and variable obscuration by circumstellar dust along the line of sight (Kiss & Bódi 2017).

V382 Aur. This target displays an RVb phenomenon in the RV phase curve (see Table 2) and emission from carbonaceous dust in the IR spectra from Spitzer (polycyclic aromatic hydrocarbons and C_{60} fullerenes; Gielen et al. 2011a).

R Sct. The distribution of gas and dust around this target was mapped in 12 CO J=2-1 using IRAM NOrthern Extended Millimeter Array (NOEMA; Gallardo Cava et al. 2021). With a NOEMA beam size of 3.12" × 2.19", CBD in R Sct was unresolved ($R \lesssim 700$ au), though the large outflow was detected ($\sim 8000 \times 15000$ au).

BD+39 4926. This target was proposed to host a dissipated disc based on low IR excess in the SED and high effective temperature (Gezer et al. 2015).

Appendix B. Summary of optical spectral visits

In this Appendix, we list all optical spectral visits considered in this study (see Table B1) for the abundance analysis of post-AGB/post-RGB binaries with faint discs (see Section 3.2).

Table B1. Spectral visits of post-AGB/post-RGB binaries with faint discs (see Section 2.3). This table is published in its entirety in the electronic edition of the paper. A portion is shown here for guidance regarding its form and content.

ObsID	MJD	Phase	RVrel
SS Gem (RV	0=-8.4 km/s, 151 visits	:)	
253252	55124.23258	0.20	2.8
260288	55160.06403	0.00	-13.6
272381	55214.99618	0.23	-3.0
273153	55221.92900	0.39	-1.1
273787	55232.98736	0.63	-7.3

Notes: RVO is the radial velocity of the spectral visit with the best S/N ratio. RVrel are radial velocities relative to visit with the best S/N ratio.

Appendix C. Master line list of the target sample

In this Appendix, we show the combined optical line list (see Table C1), which we used to derive the atmospheric parameters and elemental abundances of post-AGB/post-RGB binaries with faint discs (see Section 3.2).

Table C1. Line list of the whole studied sample of post-AGB/post-RGB binaries with full, transition, and faint discs (see Section 4). This table is published in its entirety in the electronic edition of the paper. A portion is shown here for guidance regarding its form and content.

Atomic data				W_{λ} (mÅ)			
lon	λ	log gf	χ	SZ Mon	DF Cyg		J053254
	(nm)	(dex)	(eV)	(#1)	(#2)		(#22)
С	402.9414	-2.135	7.488	-	-		-
С	422.8326	-1.914	7.685	-	-		-
С	426.9019	-1.637	7.685	-	-		-
С	437.1367	-1.962	7.685	-	-		-
С	477.0021	-2.437	7.483	-	-		-

Appendix D. Individual abundances of faint disc targets

In this Appendix, we present the derived LTE and NLTE elemental abundances of faint disc targets (see Tables D1 and D2, respectively). For more details on the abundance analysis, see Section 3.2.

Table D1. LTE [X/H] abundances of the whole studied sample of post-AGB/post-RGB binaries with full, transition, and faint discs (see Section 4).

lon	$T_{\rm cond}$	SZ Mon	DF Cyg	 J053254
	(K)	(#1)	(#2)	 (#22)
Ci	40	-0.09±0.08	0.27±0.09	 -0.42±0.06
Νi	123	$0.44 {\pm} 0.14$	-	 -
Οi	183	0.15 ± 0.11	0.73 ± 0.12	 -0.63±0.12

Note: The condensation temperatures for C and N were adopted from Lodders (2003), the condensation temperatures for all other elements were adopted from Wood et al. (2019).

Table D2. NLTE [X/H] abundances of the whole studied sample of post-AGB/post-RGB binaries with full, transition, and faint discs (see Section 4).

lon	$T_{\rm cond}$	SZ Mon	DF Cyg	 J053254
	(K)	(#1)	(#2)	 (#22)
Ci	40	-0.15±0.08	0.14±0.07	 -0.48±0.06
Νi	123	0.20 ± 0.14	-	 -
0 i	183	0.15 ± 0.11	$0.84{\pm}0.05$	 -0.62±0.12

Note: The condensation temperatures for C and N were adopted from Lodders (2003), the condensation temperatures for all other elements were adopted from Wood et al. (2019).

Appendix E. NLTE depletion profiles of full and transition disc targets

In this Appendix, we show the revised depletion profiles of full and transition disc targets (see Figures E1, E2, E3). To ensure consistency across the full, transition, and faint disc samples, we adopted the LTE abundances and luminosities of the full and transition disc targets from Mohorian et al. (2024) and Mohorian et al. (2025), which were derived using the same methodology as in this study (see Section 3.2). However, for a uniform NLTE analysis across all targets, we recalculated NLTE corrections for full and transition disc samples using pySME. These new corrections were applied to the published LTE abundances using the same procedure as for the faint disc sample (see Section 3.3). For more details on the depletion profiles of full and transition disc targets, see Section 4.1.

We note that for transition discs, the NLTE abundances derived in this study generally agree with those presented in Mohorian et al. (2025) within typical uncertainties of \sim 0.15 dex, with a median difference of 0.07 dex and an average difference of 0.10 dex. These discrepancies largely arise from two factors: (i) the need to interpolate or extrapolate NLTE corrections near the edges of the MARCS grid, which is irregular and incomplete in the

parameter space relevant to post-AGB/post-RGB binaries, and (ii) adoption of different approaches for estimating NLTE corrections (Mohorian et al. 2025, matched LTE and NLTE equivalent widths; in this study, we matched LTE and NLTE synthetic spectra). We also note that within the post-AGB/post-RGB sample, the average NLTE corrections for volatile elements (including C, N, O, and S) are ≈ -0.07 dex, whereas the average NLTE corrections for refractory elements (including Al, Si, Ti, and Fe) are $\approx +0.08$ dex. This confirms that, while NLTE corrections are essential for deriving precise individual abundances, these corrections have a minor impact on the general distributions of depletion parameters.

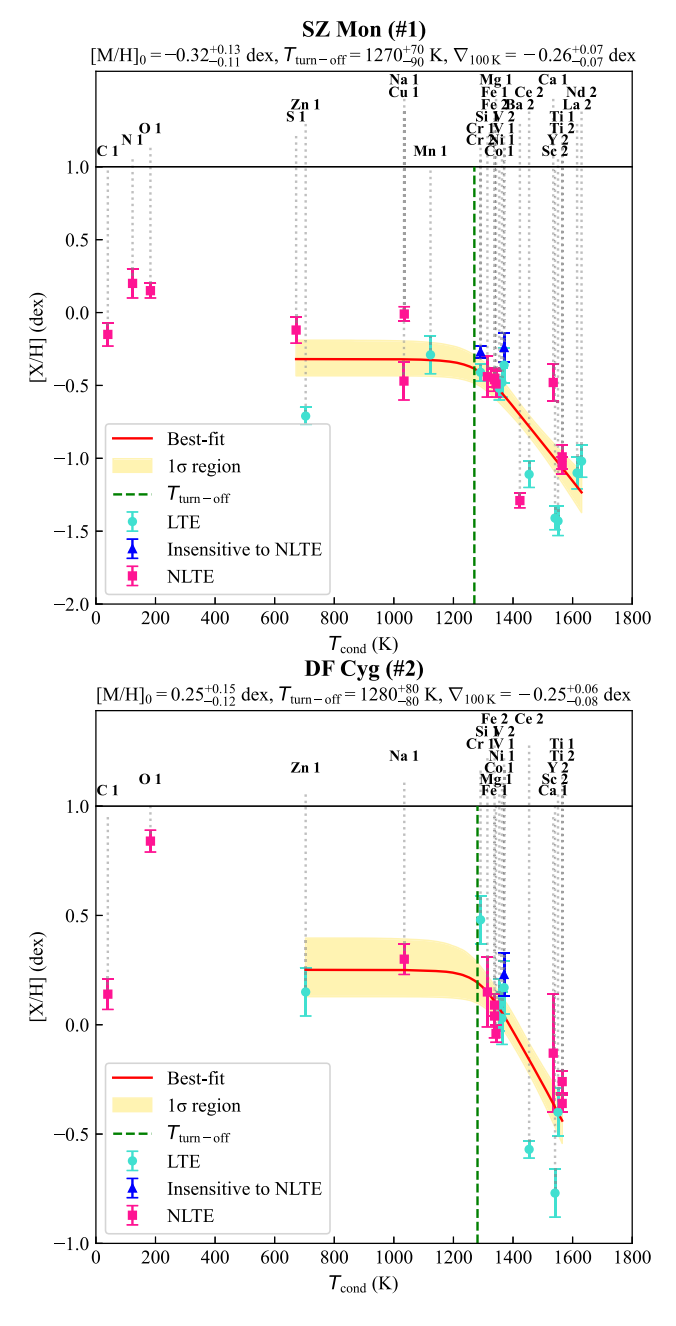


Figure E1. Elemental abundances of a subsample of post-AGB/post-RGB binaries with full discs as functions of condensation temperature (Lodders 2003; Wood et al. 2019). The legend for the symbols and colours used is included within the plot. 'NLTE insensitive' abundances are derived from spectral lines of V ii and Cr ii; for more details, see Section 3.2).

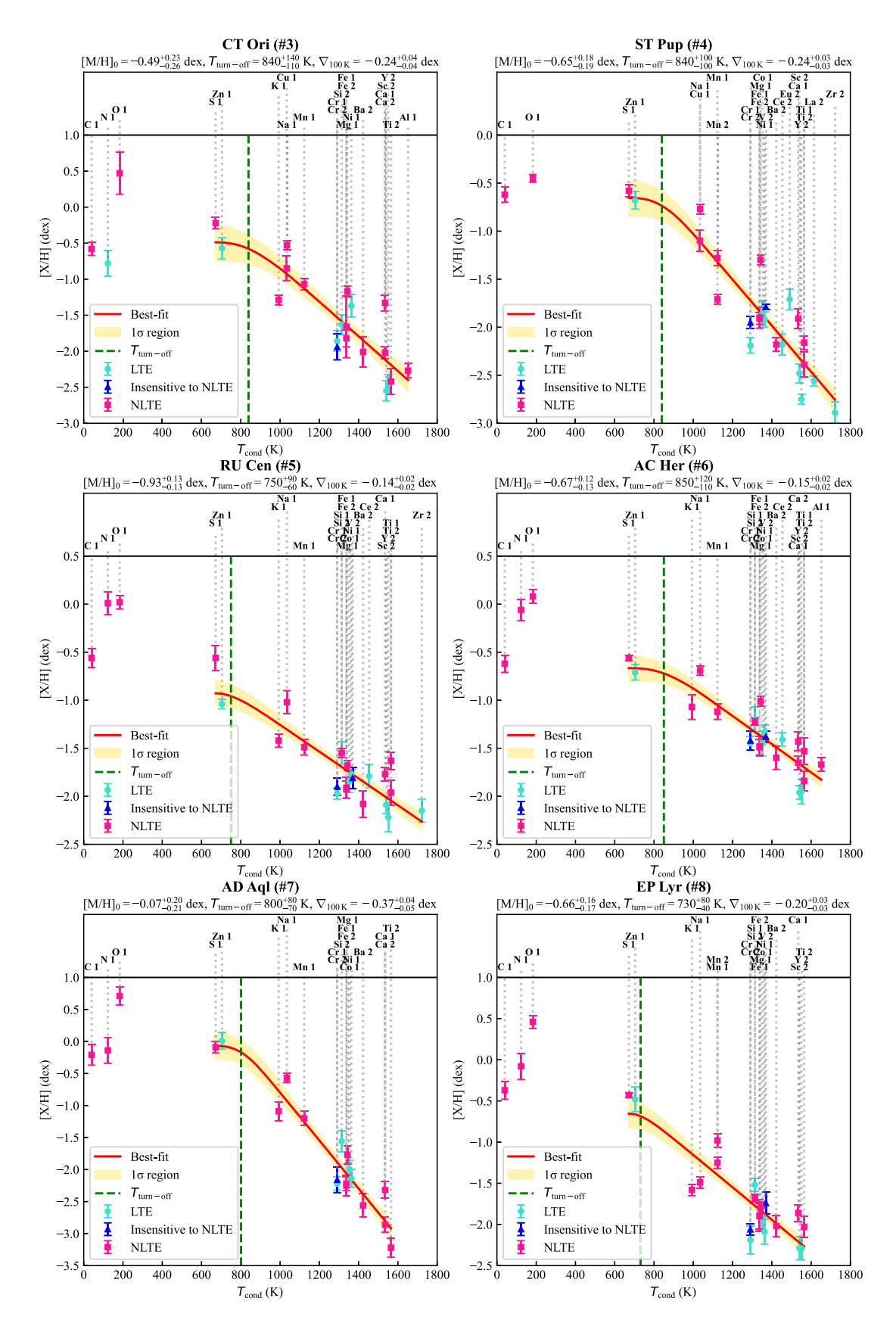


Figure E2. Elemental abundances of a subsample of post-AGB/post-RGB binaries with full and transition discs as functions of condensation temperature (Lodders 2003; Wood et al. 2019). The legend for the symbols and colours used is included within the plot. 'NLTE insensitive' abundances are derived from spectral lines of V ii and Cr ii; for more details, see Section 3.2).

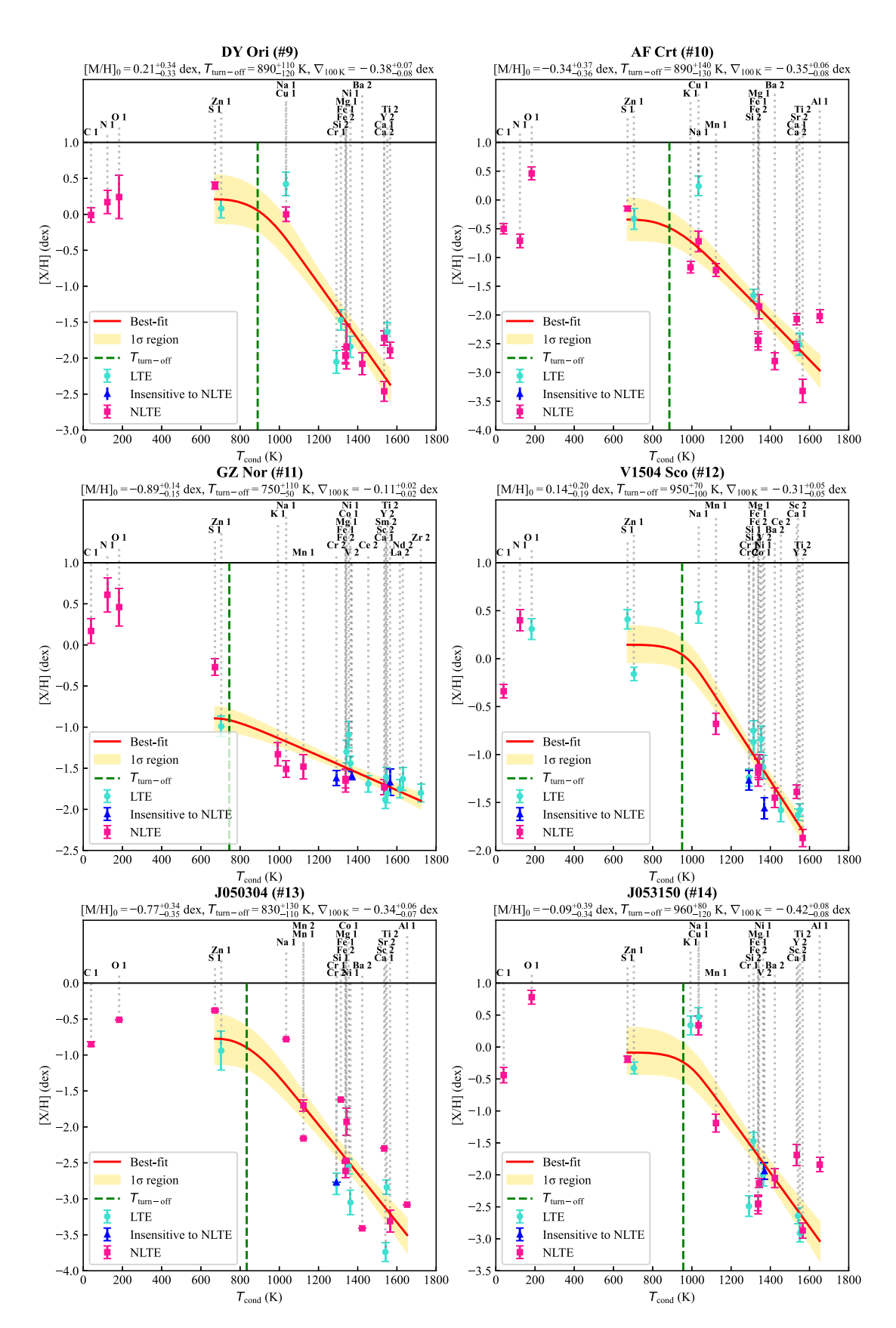


Figure E3. Elemental abundances of a subsample of post-AGB/post-RGB binaries with transition discs as functions of condensation temperature (Lodders 2003; Wood et al. 2019). The legend for the symbols and colours used is included within the plot. 'NLTE insensitive' abundances are derived from spectral lines of V ii and Cr ii; for more details, see Section 3.2).